Novel miniaturized ring resonator and metamaterial filters for UHF applications

by

José Roberto Reyes Ayona

A Thesis Submitted to the Program in Electronics Science, Electronics Science Department in partial fulfillment of the requirements for the degree of

MASTER OF SCIENCES
WITH THE SPECIALTY IN ELECTRONICS

at the

National Institute of Astrophysics, Optics and Electronics
February 2010,
Tonantzintla, Puebla

Advisor:

Dr. Alonso Corona Chávez,
Electronics Department, INAOE

Dr. Devata Venkata Bhyrava Murthy,
GTM, INAOE

Abstract

Emerging applications such as wireless communications continue to challenge RF/microwave filters with ever more stringent requirements as: smaller size, lighter weight, and lower cost. Ring resonators have been widely studied in the literature of filter applications because they are cheap and of easy fabrication. Due to the large size of these resonators, various techniques have been suggested in the literature to achieve miniaturization. Two main parameters which affect the frequency response of the ring resonators are the differences in the substrate's thickness and tolerances in the dielectric constant of the substrate. A new miniaturization technique is introduced in this thesis. This novel technique is based on the use of vias to ground and interdigital capacitors. Vias to ground allow size reduction and eliminate harmonics. The addition of the interdigital capacitor to the electromagnetic structure greatly reduces the sensitivity to substrate thickness. The resulting resonators are highly miniaturized, cheap, of easy fabrication, of low sensibility to differences in the substrate's thickness, and independent of the excitation orientation. Ultra High Frequency filters based on these novel electromagnetic ring resonant structures are presented.

The growth of interest in metamaterials has recently led to novel and interesting theoretical possibilities for microwave, infrared and optical applications. One advantage of metamaterial structures is the size reduction. In this thesis, the design of a metamaterial (MTM) transmission line based on the negative magnetic coupling using the planar technology is presented. A spiral inductor and interdigital capacitor are used as basic elements to realize the MTM transmission line. Simulations are done using the full-wave simulator SONNET and measurements are perform using the Agilent PNA series microwave vector network analyzer (E8361A).

Resumen

Las comunicaciones inalámbricas emergentes requieren que los filtros de microondas sean cada vez más pequeños, más ligeros y más baratos. Ya que son baratos y de fácil fabricación los resonadores de anillo han sido ampliamente estudiados en la literatura para aplicaciones de filtrado. Debido al gran tamaño de estos resonadores varias técnicas se han sugerido en la literatura para obtener miniaturización. Dos parámetros importantes que afectan la respuesta en frecuencia de los resonadores de anillo son las diferencias en el espesor del dieléctrico y las tolerancias de la constante dieléctrica del substrato. En esta tesis se propone una novedosa técnica de miniaturización, la cual está basada en el uso de una vía a tierra y un capacitor interdigital. La vía a tierra permite reducir el tamaño del resonador y elimina su segundo armónico. El capacitor interdigital reduce grandemente la sensibilidad que el resonador tiene con respecto al espesor del substrato. Los resonadores resultantes son altamente miniaturizados, baratos, de fácil fabricación, de baja sensibilidad a las variaciones del substrato y no dependen de la orientación con la cual son excitados. Usando estos novedosos resonadores se diseñan y fabrican filtros de ultra alta frecuencia.

El creciente interés en metamateriales ha llevado a novedosas e interesantes posibilidades teóricas para posibles aplicaciones en los rangos de microondas, infrarrojo y óptico. Una de las ventajas de los metamateriales es la reducción de tamaño. En esta tesis, se presenta el diseño de una línea de transmisión metamaterial (MTM) la cual está basada en acoplamiento magnético negativo y hace uso de la tecnología planar. Los elementos básicos para realizar la línea de transmisión metamaterial son un inductor de espiral y un capacitor interdigital. Las simulaciones son hechas en el simulador de onda completa SONNET y las mediciones realizadas con el analizador de redes vectoriales Agilent PNA (E8361A).

Index

Chapter I

Introduction

Ring resonators have been widely studied in the literature for filter applications. A ring resonator consists of a 360° closed-loop transmission line where a full-wavelength standing wave is excited. Due to the large size of these resonators, different techniques have been suggested in the literature to achieve miniaturization. In this work a new miniaturization technique is proposed by using a via to ground and an interdigital capacitor. Furthermore, it is well known that microwave resonators performance is very sensitive to tolerances in substrate thickness, which increases the tuning requirement of filters. In this work, it is shown that the addition of the interdigital capacitor reduces the resonators sensitivity to substrate thickness to about 1/7 of the original sensitivity. A 2-pole Butterworth and Chebyshev filters using the novel ring resonator are presented. The filters have fractional bandwidths of 6.1% and 14.6% and they are centered at f_0= 0.53 and f_0= 0.38 GHz respectively. In addition, a 4-pole quasi-elliptic filter (with a fractional bandwidth of 11% and center frequency of 0.53 GHz) using the highly miniaturized ring resonator is presented. Full design procedure, simulation and experimental results of the miniaturized filters are presented.

Since the first practical demonstration on negative refractive index, metamaterial structures have been widely studied and proposed. A metamaterial is an artificial material which has negative permittivity and permeability in a specific frequency range. The first metamaterial structures are impractical for filter applications because their insertion losses in the allowed band are too high. Moreover, those structures are not compatible with planar circuit technology. The first planar metamaterial structures is based on the transmission line loaded with series capacitor and shunt connected

inductors [1]. Afterwards, planar metamaterial structures based on split ring resonators came into play for application in microwave bandpass filters [2]. Soon after, complementary split ring resonators were used for filter applications on planar technology [3]. In this work a metamaterial structure using planar technology is presented. This structure is based on a theoretical metamaterial unit-cell with serial capacitors connected to magnetically negative-coupled inductors [4]. This metamaterial transmission line is implemented in planar technology using the interdigital capacitor and spiral inductor and has metamaterial behavior for the desired band. A detailed design procedure, simulations and measurements are presented along with an effective parameter extraction procedure.

1.1 Objective

The objectives of this thesis are:

1) To find a compact, inexpensive, easily fabricated and low sensitivity to substrate thickness resonating structure based on ring resonators and to use this structure to develop various kinds of UHF filters.

2) To design and fabricate a metamaterial transmission line with negative magnetic coupling using the planar technology.

1.2 Organization of this thesis

In chapter II, the current state of the art of ring resonators and metamaterials are presented.

Chapter III deals with the introduction of novel square ring resonators with via to ground and interdigital capacitor. The advantages of this novel ring resonator and the filters based on this resonator are also explained.

Chapter IV presents a complete design procedure for a Quasi-elliptic filter using the proposed ring resonator structure.

Chapter V shows the design of a metamaterial transmission line based on negative magnetic coupling using planar technology (series capacitors and magnetic-coupled inductors).

Finally, all the conclusions obtained from this thesis are mentioned in Chapter VI.

Chapter II

Literature on ring resonators and metamaterials

In this chapter, the current state of the art of the filters based on the ring resonators and metametarials is discussed. A detailed explanation on the microstrip ring resonator, modes of these resonators, and the available literature on the filters based on the ring resonators are presented. A brief review on the recent study of the metamaterials, applications of the metamaterials and the available literature on metamaterials are shown.

2.1 Ultra High Frequency (UHF) applications

Wireless communications systems have had an explosive evolution in the last years. Wireless systems are attractive because they are compact and avoid the usage of cumbersome wires. The electromagnetic spectrum is divided into several bands; one of them is Ultra High Frequency (UHF). UHF band has a frequency range from 0.3 GHz to 4 GHz (1–0.075 m), also called decimeter band. This band is divided into L-Band (1–2 GHz) and S-Band (2–4 GHz). Most applications of these frequencies are: television, cellular telephony, local area networks (LANs) (Bluetooth, Zigbee, Wi-Fi), global positioning systems, radar operation, cordless telephones, automotive applications, satellite applications (control frequencies, time signals, meteorology, mobile communications, earth exploration, radio localization, radio diffusion), radio-astronomy, and aeronautics.

2.2 Microstrip ring resonators

Wolff and Knoppik [5] explained the field theory of the ring resonator which describes the curvature effect on the ring resonant frequency using the magnetic-wall model. The resonant frequency of the ring resonator mainly depends on its dimensions and they are related as $2\pi r = n\lambda_g$, where r is the mean radius of the ring resonator, λ_g is the guided-wavelength and n (an integer) is the mode number. The ring resonator is a simple circuit that has an integral multiple of guided wavelength which is equal to the mean circumference. Many complicated circuits can be derived using this simple resonator structure by cutting a slit, adding a notch, cascading two or more rings, placing multiple input and output lines, etc. It is very difficult to use the magnetic wall model to obtain the frequency modes of the square ring resonator due to its complex boundary conditions; as a consequence the square ring resonator has not a proper field theory derivation for its frequency modes, just as the annular ring resonator. The magnetic-wall model does not explain the dual-mode behavior very well. The magnetic wall model considers the ring as a cavity resonator with electric walls on the top and bottom and magnetic walls on the sides. It is assumed that there is no z-dependency and that the fields are transverse magnetic (TM) in the z direction. A solution of Maxwell's equations in cylindrical coordinates is

$$E_Z = AJ_n(kr) + BN_n(kr)\ \cos(n\phi) \tag{2.1a}$$

$$H_r = \frac{n}{j\omega\mu_0 r}\ AJ_n(kr) + BN_n(kr)\ \sin(n\phi) \tag{2.1b}$$

$$H_\phi = \frac{k}{j\omega\mu_0}\ AJ_n'(kr) + BN_n'(kr)\ \cos(n\phi) \tag{2.1c}$$

where A and B are constants, k is the wave number, ω is the angular frequency, J_n is a Bessel function of the first kind of order n, and N_n is a Bessel function of the second kind of order n. J_n' and N_n' are the derivatives of

the Bessel functions with respect to the argument (*kr*). The boundary conditions are

$$H_\phi = 0 \qquad \text{at} \qquad r = r_0 \tag{2.2a}$$

$$H_\phi = 0 \qquad \text{at} \qquad r = r_i \tag{2.2b}$$

where r_0 and r_i are the outer and inner radii of the ring. This leads to the eigenvalue equation

$$J_n^{'}(kr_0)N_n^{'}(kr_i) - J_n^{'}(kr_i)N_n^{'}(kr_0) = 0 \tag{2.3}$$

where

$$k = \omega\sqrt{\varepsilon_0\varepsilon_r\mu_0} \tag{2.4}$$

The resonant frequency of the ring resonator is calculated by using the outer and inner radii, r_0 and r_i of the ring.

2.2.1 Frequency modes for ring resonators

A transmission-line model which is unaffected by boundary conditions is used to calculate the frequency modes of annular and square ring resonators [5]. Figure 2.1 presents the one-port configuration of square and annular ring resonators. For a ring of any general shape, the total length *l* can be divided into l_1 and l_2 sections.

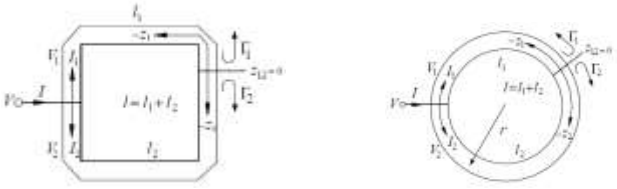

(a) (b)

Figure 2.1. (a) Schematic of the one port square ring resonator and (b) annular ring resonator [6].

For square ring resonators, the sections are considered to be transmission lines of Z_1 *and* Z_2 impedance. The voltages and currents of both sections for a lossless transmission line are

$$V_{1,2}(Z_{1,2}) = V_0^+(e^{-j\beta_{Z_{1,2}}} + \Gamma_{1,2}(0)e^{j\beta_{Z_{1,2}}}) \quad (2.5a)$$

$$I_{1,2}(Z_{1,2}) = \frac{V_0^+}{Z_0}(e^{-j\beta_{Z_{1,2}}} - \Gamma_{1,2}(0)e^{j\beta_{Z_{1,2}}}) \quad (2.5b)$$

where $V_0^+e^{-j\beta_{Z_{1,2}}}$ is the incident wave propagating in the $+Z_{1,2}$ direction, $V_0^+\Gamma_{1,2}(0)e^{j\beta_{Z_{1,2}}}$ is the reflected wave propagating in the $-Z_{1,2}$ direction. $\Gamma_{1,2}(0)$ is the reflection coefficient at $Z_{1,2} = 0$, and Z_0 is the characteristic impedance of the ring.

Standing waves set up on the ring when a resonance occurs. The shortest length of the ring resonator that supports these standing waves can be obtained from the positions of the maximum values of these standing waves. These positions can be calculated from the derivatives of the voltages and currents in Equation (2.5). The derivatives of the voltages are

$$\frac{\partial V_{1,2}(Z_{1,2})}{\partial Z_{1,2}} = -j\beta V_0^+\left[e^{-j\beta_{Z_{1,2}}} - \Gamma_{1,2}(0)e^{j\beta_{Z_{1,2}}}\right] \quad (2.6)$$

Substituting $\Gamma_{1,2}(0) = 1$ into equations (2.5), the voltages and currents can be obtained as

$$V_{1,2}(Z_{1,2}) = 2V_0^+\cos(\beta Z_{1,2}) \quad (2.7a)$$

$$I_{1,2}(Z_{1,2}) = -\frac{j2V_0^+}{Z_0}\sin(\beta Z_{1,2}) \quad (2.7b)$$

From equations (2.7) the absolute values of voltage and current standing waves are shown in Figure 2.2. From Figure 2.2, it is observed that the standing waves repeat for multiples of $\lambda_g/2$ on each section of the ring. In order to have the standing waves, the shortest section length has to be $\lambda_g/2$, which can be treated as the fundamental mode of the ring. For higher order modes,

$$l_{1,2} = n\frac{\lambda_g}{2} \quad \text{for } n = 1, 2, 3,\ldots \tag{2.8}$$

where n (an integer) is the mode number.

The total length of the square ring resonator l is

$$l = (l_1 + l_2) = n\lambda_g \tag{2.9}$$

or in terms of annular ring

$$l = n\lambda_g = 2\pi r \tag{2.10}$$

where r is the mean radius

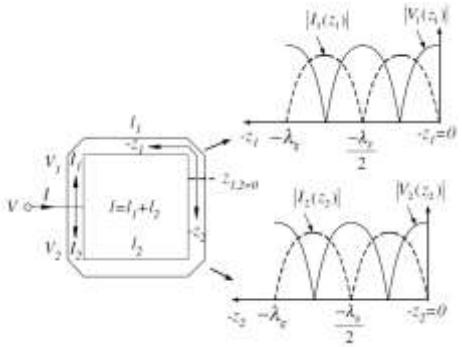

Figure 2.2. Standing waves on each section of the square ring resonator [6].

2.2.1.1 Modes of ring resonators

The modes of the ring resonators can be obtained by different types of excitation and perturbation. The resonant modes of a coupled ring are divided into three types based on the type of excitation and perturbation: (1) regular mode, (2) forced mode (or excited mode), and (3) split mode.

1. Symmetric input and output feed lines excite the regular modes. Figure 2.3 shows the voltage maxima (x) for the first and second modes of the ring, due to the capacitive feed coupling. The voltage maxima are present at 0 and 180°, and they will be present at the same place for higher order modes

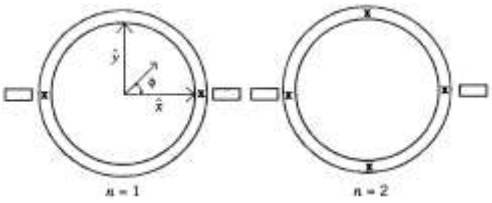

Figure 2.3. Voltage maxima for the two first modes of a ring [6].

2. The forced modes can be obtained by an open or a short. Gaps on the ring create an open type, due to the capacitive nature of an open there will be a voltage maximum where the open is placed. A thin conductor sheet on the substrate is used to create a short, the short will change the boundary conditions forcing equal voltages on both sides of the short being the resulting voltage values the minimum. When the open or short are located at an angle of ±90°, the standing wave patterns for even mode numbers will have minimum voltage values at the input and output feed lines; as a consequence there will be no energy transfer between input and output ports. For this reason, only odd mode numbers can exist in these forced modes. If the gap is located at 0 or 180° the ring will have regular resonant modes.

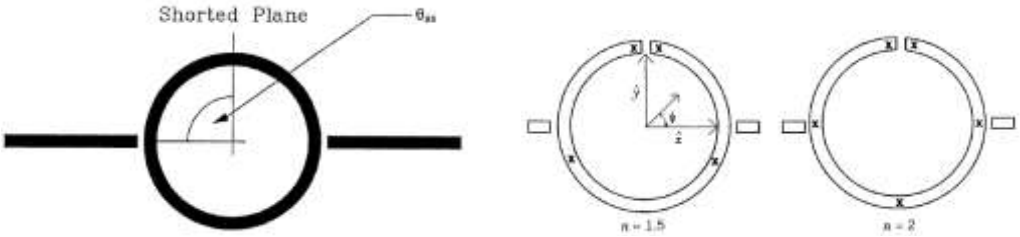

(a) (b)

Figure 2.4. (a) Short and (b) open annular ring resonators [6].

3. Wolff [7] explained the split resonant mode in ring resonators, the split mode can be obtained with two different techniques: 1) Asymmetric feed lines, as its name implies this technique is based on asymmetric external excitation. Let's consider the feed lines are placed at 180 and 0° as shown in Figure 2.4(a), an asymmetric feeding can be obtained by moving any of the feed lines to a different angle position. In other words, when the angle between the feeding lines is not 180°, a split mode is obtained. 2) A split mode can be achieved by using the notch perturbations. When the microstrip line of the ring is wider or narrower at some regions of the ring, a split mode is obtained. The notch perturbation technique is based on the different characteristic impedances that a ring will have when its microstrip line width is not the same for the entire ring.

2.3 UHF Filters

Many miniaturization techniques have been reported for filter applications. In [8] a coupling gap elliptic-function band pass filter with microstrip ring resonator is presented. The ring is fed by a coupling gap at one port, and a tapped line at the other port. Figure 2.5 shows the layout of the filter. The perturbed stub is used for exciting the dual mode, the physical length of the ring is λ.

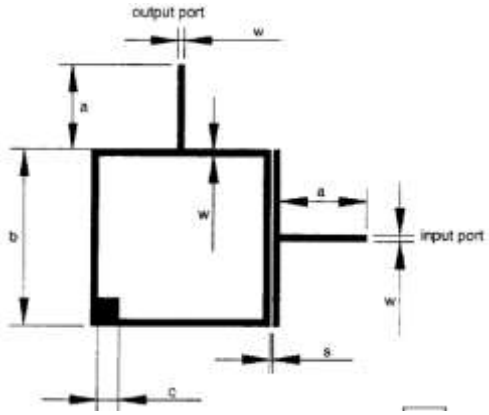

Figure 2.5. Structure of one coupling gap elliptic-function bandpass filter [8].

A filter with four identical arms and a square patch attached to an inner corner of the internal ring is presented in [9], the internal ring is attached to an external square closed ring by each one of its corners. Figure 2.6 shows the structure of this filter, the four gaps on the internal ring increase the capacitance resulting in size reduction. The filter consists of two square rings one inside the other, the square patch allows degenerate modes.

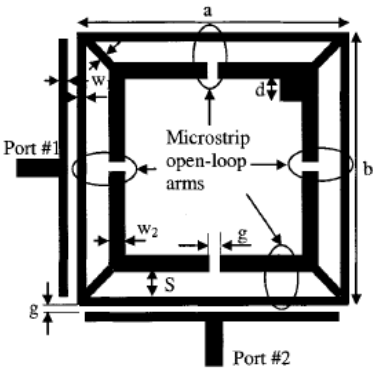

Figure 2.6. Dual-mode microstrip filter [9].

A microstrip ring resonator using L-shape coupling arms is reported in [10]. The ring is fed by two orthogonal feed lines, the lines are connected to an L-shape coupling arm as it is shown in Figure 2.7(a). The tuning stub extends the coupling stub to increase the coupling periphery. The asymmetrical structure perturbs the field of the ring resonator and excites two degenerate modes. Figure 2.7(b) shows the schematic of the L-shape feeding line.

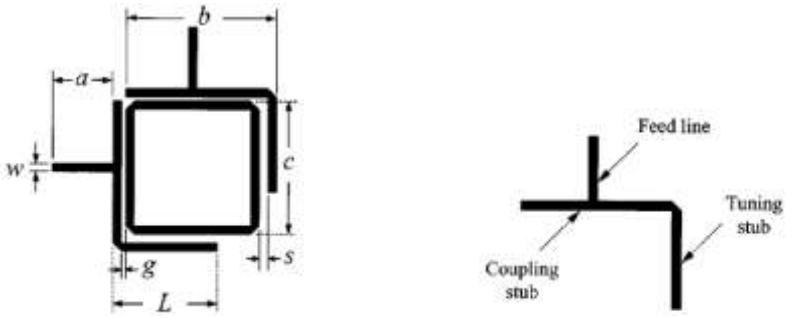

(a) (b)

Figure 2.7. Bandpass filter. (a) Layout. (b) L-shape coupling arm [10].

2.4 Metamaterials

EM response in homogeneous materials is predominantly governed by two parameters. One of these parameters, $\varepsilon(\omega)$, describes the response of a material to the electric component of light (or other EM wave) and the other, $\mu(\omega)$, to the magnetic component at a frequency ω. Both of these parameters are typically frequency-dependent complex quantities, and thus there are in total four numbers that completely describe the response of an isotropic material to EM radiation at a given frequency,

$$\varepsilon(\omega) = \varepsilon_1(\omega) + j\varepsilon_2(\omega) \tag{2.11a}$$

$$\mu(\omega) = \mu_1(\omega) + j\mu_2(\omega) \tag{2.11b}$$

For most materials, the two complex quantities ε and μ are the only relevant terms and hence dictate the response between electromagnetic wave and matter. Among the various fields of science, however, there are many other EM parameters used to describe the wave propagation that are related to the material parameters shown in equation 2.11 by simple algebraic relations; for example such quantities as the absorption or the conductance of a material can be redefined in terms of ε and μ.

A commonly used EM parameter is the index of refraction, which is defined as $n(\omega)^2 = \varepsilon(\omega)\mu(\omega)$. The index of refraction provides a measure of the speed of an EM wave as it propagates within a material.

In virtually all the text books on the subject of optics or electricity and magnetism the refractive index is always assumed positive. But nature has hidden a great secret from us, first described by Russian physicist Victor Veselago [11]. Veselago realized that if a material were found that had negative values for both the electric and magnetic response functions, (i.e. $\varepsilon(\omega) < 0$ and $\mu(\omega) < 0$), then its index of refraction would also be negative, $n(\omega) < 0$. Although Veselago conjectured that naturally occurring materials with negative refractive index might be found or synthesized in naturally occurring materials, such materials have never been found. However, because artificially structured materials can have controlled magnetic and electric responses over a broad frequency range, it is possible to achieve the condition $\varepsilon < 0$ and $\mu < 0$ in artificial composites and Veselago's hypothesized material can, indeed, be realized. These artificially structured composites are known as metamaterials.

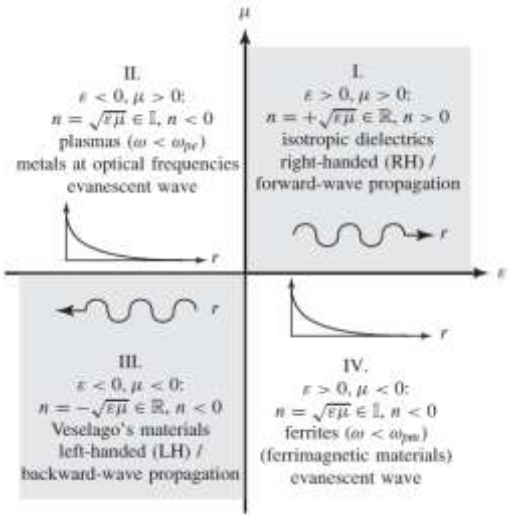

Figure 2.8. Permittivity-permeability (ε-μ) and refractive index (n) diagram [12].

A definition for metamaterial (MTM) is "*artificial effectively homogeneous electromagnetic structures with unusual properties not readily available in nature"* [12]. There are four possible sign combinations for the pair (***ε***, ***μ***). These combinations are shown in Figure 2.8.

Progress in the metamaterials has been rapid, MTM structures have negative behavior just for a limited frequency range. Different structures have been implemented for different frequency ranges. The scaling of artificial structures has already been demonstrated from radio frequencies to millimeter-wave, far infrared, mid-infrared, and near infrared wavelengths, spanning nearly seven orders of magnitude in frequency and they are shown in Figure 2.9.

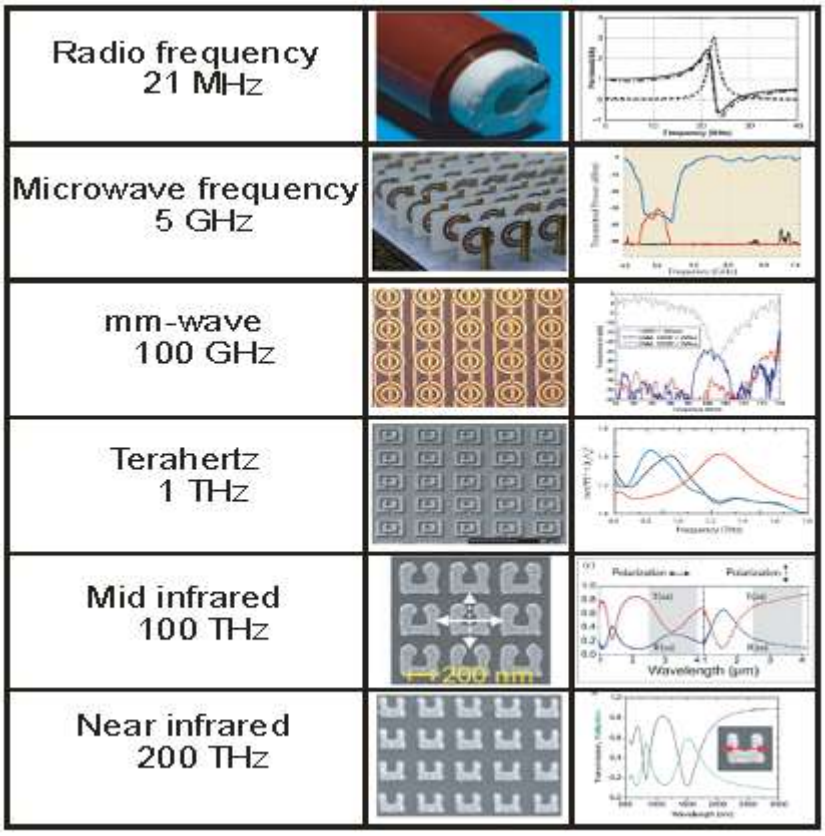

Figure 2.9. Demonstrated MTM works from RF to near optical frequencies [13].

LH media were predicted by Veselago [11] and it challenged the several fundamental phenomena:

1. Reversal of Doppler effect (shown in Figure 2.10(a))

2. Reversal of Vavilov-Cerenkov radiation (shown in Figure 2.10(b))

3. Reversal of Snell's law (shown in Figure 2.11(a))

4. Reversal of Goss-Hänchen effect. (shown in Figure 2.11(b))

5. Reversal of the boundary conditions relating the normal components of the electric and magnetic fields at the interface between a conventional/RH medium and a LH medium (shown in Figure 2.12 and 2.13)

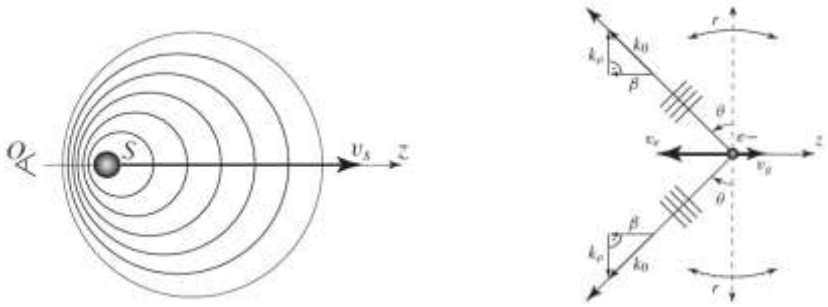

(a) (b)

Figure 2.10. Reversed phenomena in LH MTMs (a) Doppler effect and (b) Vavilov-Cerenkov radiation [12].

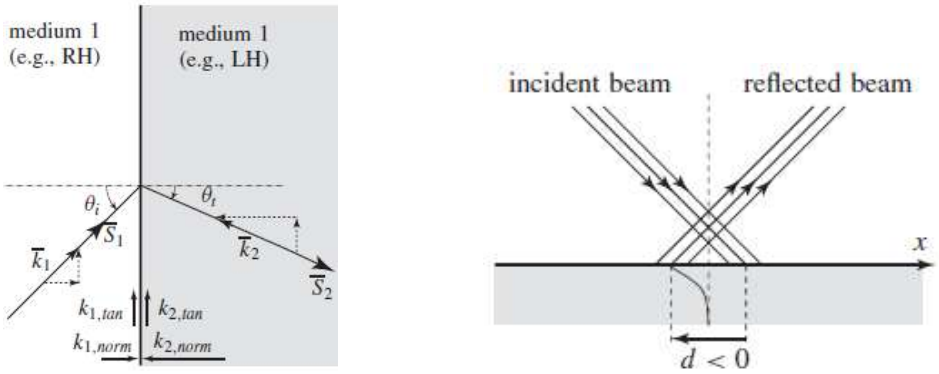

(a) (b)

Figure 2.11. Reversed phenomena in LH MTMs (a) Snell's law and (b) Goss-Hänchen effect [12].

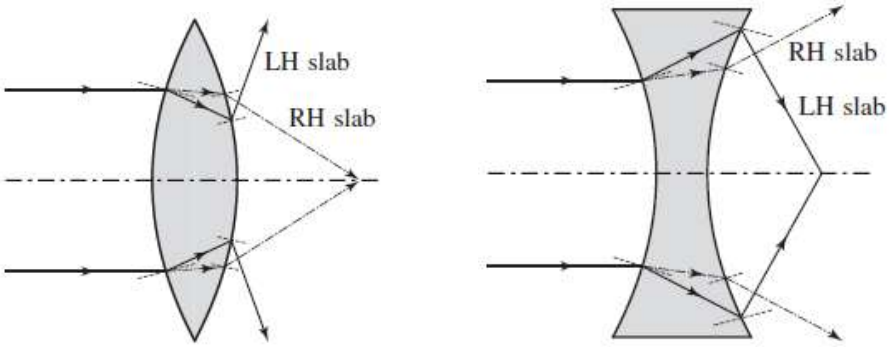

Figure 2.12. Reversed lensing effect phenomena in LH MTMs [12].

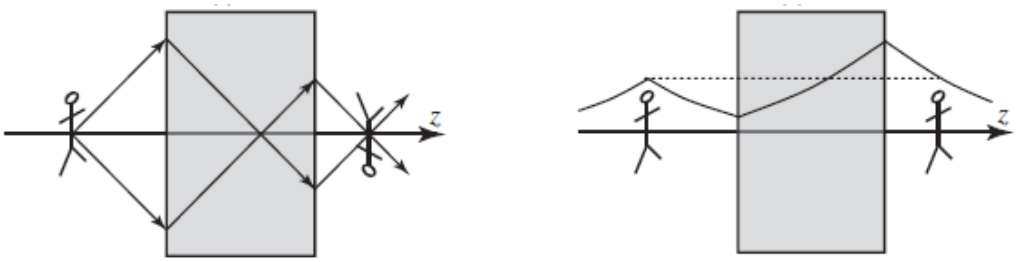

Figure 2.13. Reversed subwavelength focusing phenomena in LH MTMs [12].

Shelby *et al.,* [14] reported the first practical demonstration on a negative refractive index and as a consequence the first practical artificial MTM structure. Negative refractive index transmission line implementations [15-18] which demonstrated sub-wavelength imaging and focusing were reported later. Metamaterial structures are based on two different techniques 1) split-ring resonators and thin wires and 2) loaded transmission lines. Novel RF/microwave devices such as phase-shifters [19, 20], delay lines [21], waveguides [22], antennas [17, 23], stealth technology structures [24], power dividers [25], filters [26, 27], and couplers [28] have been implemented using these techniques.

Chapter III

Miniaturized Ultra High Frequency (UHF) filters using square ring resonators

In this chapter, miniaturized filters based on the square ring resonator (with via to ground) and interdigital capacitor are presented. At first, the introduction of square ring resonators and the effect of vias in these resonators are explained. Sensitivity analysis on substrate thickness is performed to choose the square ring resonators with the lowest sensitivity. Subsequently, the design procedure of Butterworth and Chebyshev filters using very-low-sensitivity square ring resonators are shown. Finally, the simulation and measurement results of the proposed filters using the resonators are presented.

3.1 Square ring resonators

There is a present desire for compact communication devices; a microstrip resonator is popular not just for its compact size, but also because of its high quality factor, sharp rejection, and low cost. The ring resonator is merely a transmission line formed in a closed loop, when the mean circumference of the ring is equal to an integral multiple of a guided wavelength a resonance is established. This can be expressed as $2\pi r = n\lambda_g$ (for n = 1,2,3,…), where r is the mean radius of the ring in meters, λ_g is the guided wavelength in meters, and n (an integer) is the mode number. This equation can be applicable to square rings, where l substitutes $2\pi r$ (l is the mean perimeter of the ring in meters). A schematic of the square ring resonator is shown in Figure 3.1. The

use of a forced-mode technique can result in the reduction of the ring resonant frequency value.

Introduction of via to ground in the square ring resonator helps in removing a voltage maximum, this affects the resonant frequency of the resonator. Various ring resonators with via to ground were simulated using a full-wave EM simulator [29]. The via to ground was placed at a different position for each simulated ring resonator. Figure 3.1(a) & (b) depict the schematic of the square ring resonator with and without a via. Microstrip coupling is used for the excitation of the resonators. In order to have weak coupling at the input and output ports of the resonator the feed lines are kept distant from the ring to ensure that the resulting resonance is mainly due to the ring physical characteristics.

If the via to ground is not present in the circuit shown in Figure 3.1(b), two voltage maxima would exist on the ring, one located where the via is, and the other at the opposite side of the ring. Figure 3.2 shows the current distribution at the resonant frequency of the ring resonators with and without via. The difference between the standing wave patterns is clearly observed. The elimination of a voltage maximum results in the decrease of the ring resonant frequency to half the original value as shown in Figure 3.3. The use of a via to ground will not only reduce the self-resonance to half the original value but also eliminates the high order resonance which is depicted in Figure 3.3. The ring resonator with via to ground resonates at 1GHz and has a higher order resonance at 3 GHz. The conventional ring resonator has its self-resonance at 2 GHz and its higher order resonance at 4 GHz. In general, the resonances for the conventional ring resonators occur at $f_r = nl$, where l is the physical length of the ring and n = 1,2,.., and for the ring resonator with via to ground at $f_r = nl/2$, where l is the physical length of the ring and n = 1,3,..,.

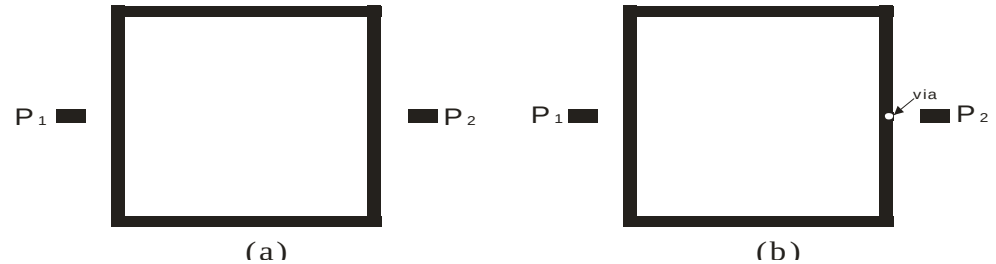

Figure 3.1. Layouts of square ring resonator (a) without via to ground and (b) with via to ground.

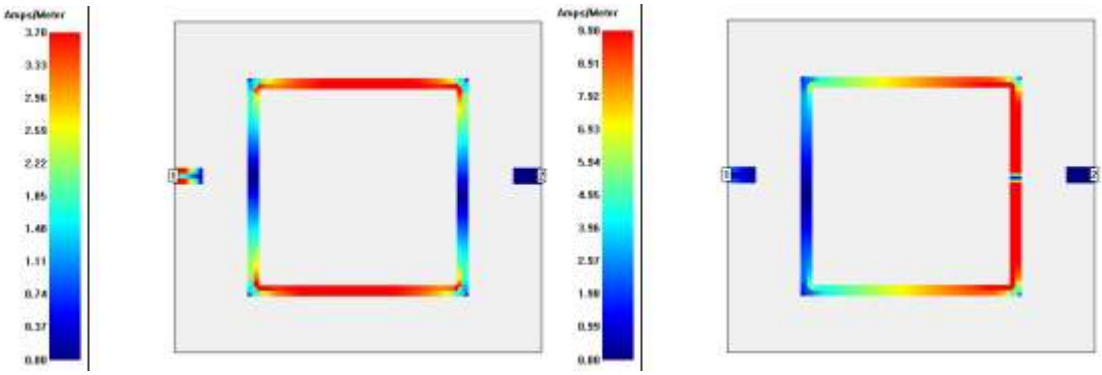

Figure 3.2. Current distributions on a square ring resonator (a) without (f_0=2 GHz) and (b) with via to ground (f_0=0.98 GHz).

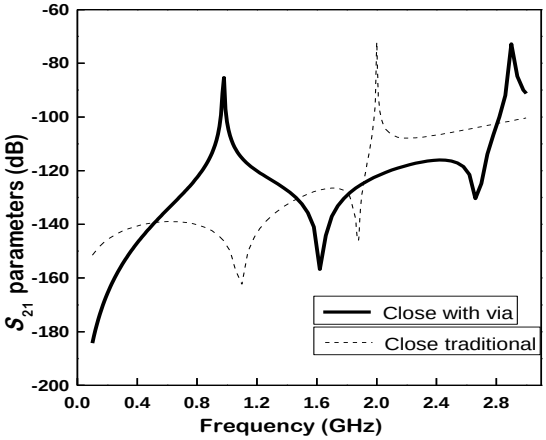

Figure 3.3. Simulated S_{21} parameters of a square ring resonator with (λ/2) and without via to ground (λ).

The advantage of using a via to ground for the square ring resonators has been shown, but the same effect is also applicable with the commonly used open ring resonator, as shown in Figure 3.4(a). The use of a via to ground is just a complex-implementation option for the open ring. The need for a better behavior of resonators with vias to ground takes us to the implementation of an open square ring resonator with a via to ground. Figure 3.4(a) shows the layout of an open square ring resonator, Figure 3.4(b) presents the same resonator with the addition of a via to ground. Figure 3.5 shows the current distributions of the resonators shown in Figure 3.4.

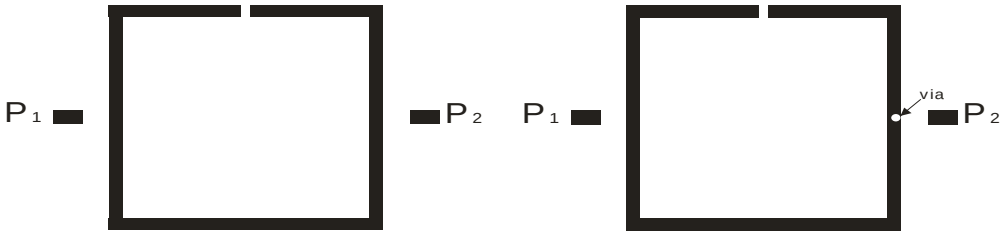

Figure 3.4. Layout of an open square ring resonator (a) without via to ground and (b) with via to ground.

It is interesting to note that the current distribution for the open square ring with a via to ground shows a spiral like behavior, and at the via there is a current maximum and a current minimum. From Figure 3.6, it is concluded that the use of a via to ground on ring resonators gives the additional advantage of size reduction compared to the conventional ring resonators.

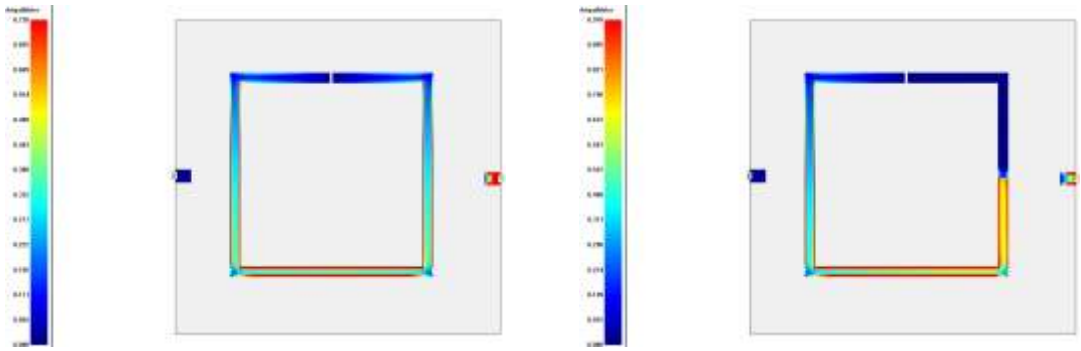

Figure 3.5. Current distribution on an open square ring resonator (a) without (f_0=0.98 GHz) and (b) with via to ground (f_0=0.66 GHz).

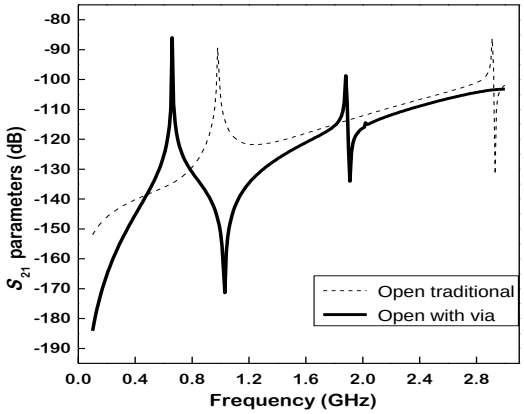

Figure 3.6. Simulated S_{21} parameters of an open square ring resonator ($\lambda/2$) and an open square ring resonator with via to ground ($\lambda/3$).

Figures 3.7 (a) and (b) show the schematics of a close ring and open ring with a via to ground and an interdigital capacitor. Figure 3.8 presents the current distributions of the resonating structures shown in Figure 3.7. The current distribution of the open ring resonator with a via to ground takes the spiral form, despite the fact that the open resonator has a capacitive effect at the slot, the voltage maximum is not at the slot as it is usually and the current intensity changes drastically from one side of the via to the other. Figure 3.9 depicts the simulated transmission coefficient response of the proposed square ring resonators. It is observed that both the resonators resonate at a lower frequency by the introduction of the interdigital capacitor. The associated resonance for the closed square ring resonator with a via to ground and an interdigital capacitor is at $\lambda/4$ and for the open square ring resonator with a via to ground and an interdigital capacitor is $\lambda/6$. The proposed resonators are the miniaturized type of ring resonators. Another advantage of the novel resonators over the traditional open square ring resonator is that the novel resonators resonate at the same frequency when are fed vertically or horizontally. Figure 3.10(a) shows the simulated S_{21} parameters of a close ring when the ring is fed horizontally and when the ring is rotated 90°. Figure 3.10(b) shows the simulated S_{21} parameters of an open ring when the ring is fed horizontally and when the ring is rotated 90°.

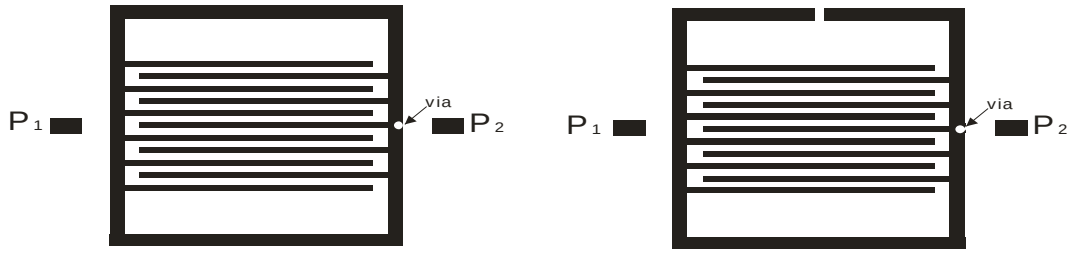

Figure 3.7. Layouts of square ring resonator with via to ground and interdigital capacitor (a) close ring and (b) open ring.

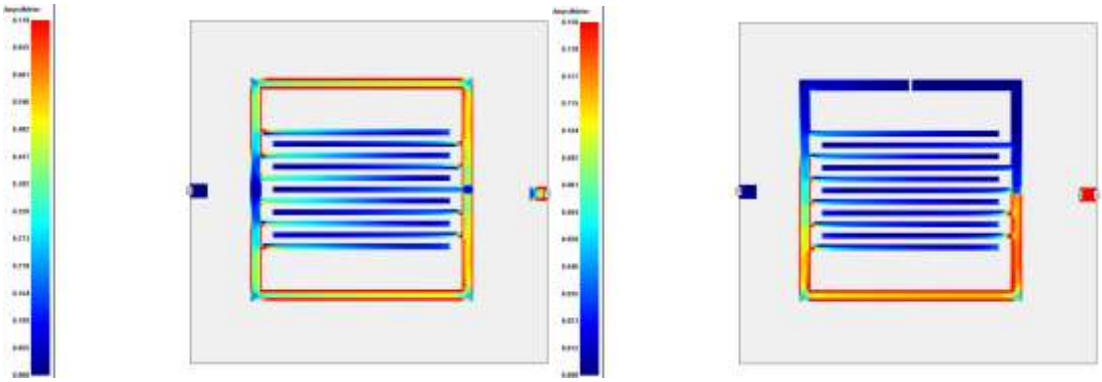

Figure 3.8. Current distributions of a square ring resonator with via to ground and interdigital capacitor (a) close ring (f_0=0.548 GHz) and (b) open ring (f_0=0.372 GHz).

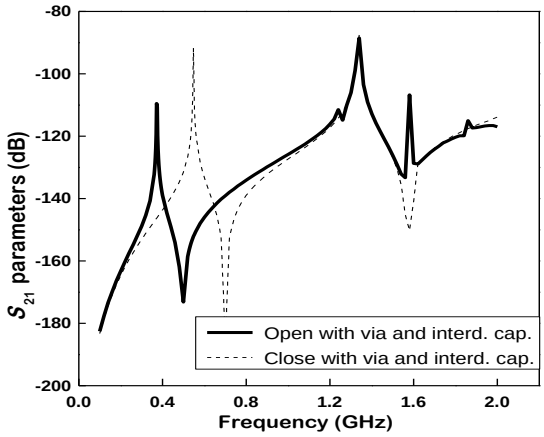

Figure 3.9. Simulated S_{21} parameters of a close square ring resonator with a via to ground and an interdigital capacitor (λ/4) and an open square ring resonator with a via to ground and an interdigital capacitor (λ/6).

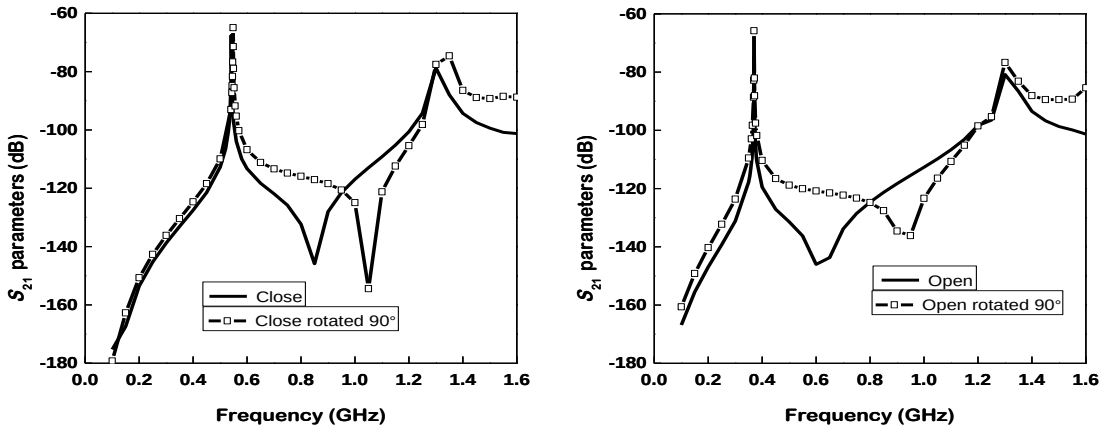

(a) b)

Figure 3.10. Simulated S_{21} parameters of rings when are fed horizontally and when the rings are rotated 90°. a) Close square rings. b) Open square rings.

3.2 Sensitivity to substrate thickness

The sensitivity to substrate thickness (SST) is "*the percent change in the resonance frequency due to the change in the substrate thickness for a microwave circuit*" [30]. SST is a very important parameter which plays a crucial role for filter applications because the response of the resonator is mainly affected by the differences in the substrate's thickness and the tolerances in the dielectric constant of the substrate. A high sensitivity would increase the tuning-time of a filter. A long tuning-time increases the manufacturing cost. A low tuning-time or nil tuning-time is desirable. Coplanar filters are known to have lower sensitivity, as compared to filters in microstrip technology. The reason is that the electric field is concentrated on the surface for coplanar filters and for this cause the resonance is little affected by the substrate tolerances. Structures with very low sensitivity to substrate thickness such as novel dual-mode ring resonators [30] and superconducting microstrip filters with double spiral inductors and interdigital capacitors [31] have been proposed.

The ratio of variation in the center frequency per millimeter of substrate variation (Δf) is given by

$$\Delta f = \frac{\Delta f_0}{\Delta h \times f_0} \times 100 \tag{3.1}$$

where Δf_0 is the variation of the resonance frequency, Δh is the variation in substrate thickness, and f_0 is given by

$$f_0 = \frac{f_{01} + f_{02}}{2} \tag{3.2}$$

where f_{01} and f_{02} are the associated resonant frequencies of the resonator with different substrate thicknesses.

In order to have low sensitivity to substrate thickness for the square ring resonators, an interdigital capacitor is introduced in the resonator. Analysis is performed by changing the substrate thickness and number of fingers in the interdigital capacitor. A square ring resonator with a via to ground at a center frequency of 1GHz is designed. RT-Duroid 6010 (ε_r = 10.8) substrate is chosen for the SST analysis. Simulations are performed in a full wave electromagnetic simulator [29] for two different dielectric substrate thicknesses (h = 1.27 mm and h = 0.635 mm) and different number of interdigital-capacitor fingers. A schematic of the proposed square ring resonator with a via, used for the simulations, is shown in Figure 3.7. The dimensions of the fingers of the interdigital capacitor are: width of line 0.4 mm, space between fingers 0.4 mm, length of lines 13.2 mm, and separation between ring and interdigital capacitor lines 0.8 mm. Figure 3.11 depicts the SST for different number of fingers in the interdigital capacitor. From the figure, it is clear that the smallest SST occurs for 11 fingers for the close square ring resonator with a via and an interdigital capacitor and the value of SST for 11 fingers is 0.46%/mm. The variation in resonant frequency for the

resonators with different substrate thickness is of 1.6 MHz. The smallest sensitivity for the open square ring resonator with a via to ground and an interdigital capacitor occurs at 15 fingers, the value of SST is 0.23%/mm. The variation in frequency for the resonators with different substrate thickness is of 0.25 MHz. The increase in the number of fingers of the interdigital capacitor increases the associated ring capacitance resulting in the decrease of the associated ring resonant frequency.

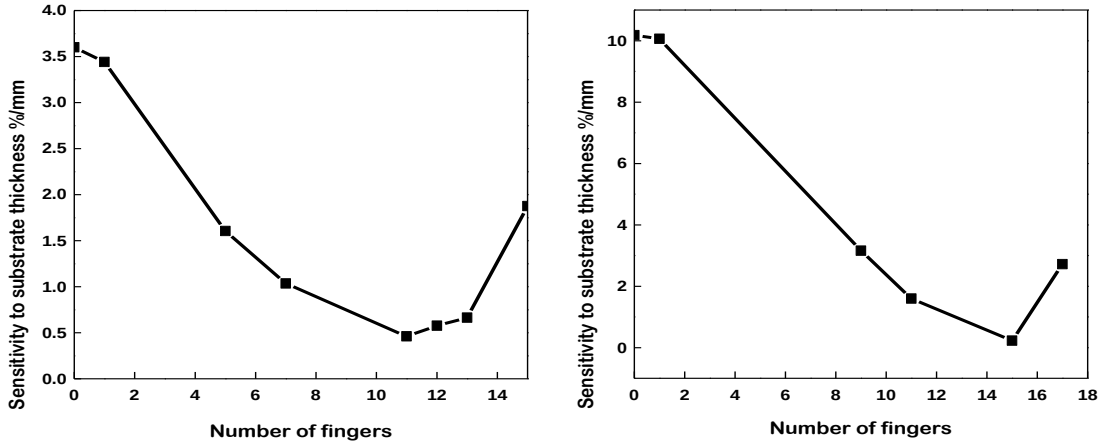

(a) (b)

Figure 3.11. SST vs. number of fingers for (a) close ring resonator (b) open ring resonator.

3.3 Design of Butterworth and Chebyshev filters using ring resonators

Most RF/microwave filters can be represented by a two-port network, where V_1, V_2 are the voltage variables and I_1, I_2 are the currents variables at ports 1 and 2, E_S is the source, and Z_{01} and Z_{02} are the terminal impedances. The two-port network and its variables are shown in Figure 3.12. For a sinusoidal voltage source at port 1, the associated signal equation is given by

$$v_1(t) = |V_1|\cos(\omega t + \phi) \tag{3.3}$$

the complex amplitude of V_1 is defined by

$$V_1 = |V_1| e^{j\phi} \tag{3.4}$$

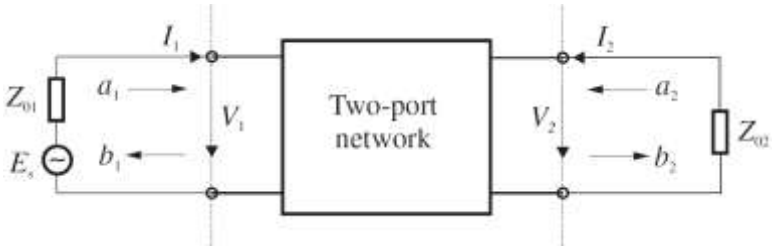

Figure 3.12. Two-port network showing network variables [32].

A network can be characterized in high frequency by measuring the reflection and transmission of an electromagnetic wave at each port. The variables a_1, b_1, a_2, and b_2 are introduced, ´a´ indicates the incident waves and ´b´ the reflected waves. The voltage and current variables are related to the wave variables by

$$V_n = \sqrt{Z_{0n}}(a_n + b_n) \tag{3.5a}$$

$$I_n = \frac{1}{\sqrt{Z_{0n}}}(a_n - b_n) \tag{3.5b}$$

$$a_n = \frac{1}{2}\left(\frac{V_n}{\sqrt{Z_{0n}}} + \sqrt{Z_{0n}} I_n\right) \tag{3.5c}$$

$$b_n = \frac{1}{2}\left(\frac{V_n}{\sqrt{Z_{0n}}} - \sqrt{Z_{0n}} I_n\right) \tag{3.5d}$$

for n = 1 and 2

The S or scattering parameters of a two-port network in terms of the wave variables are defined as

$$S_{11} = \frac{b_1}{a_1}\bigg|_{a_2 = 0} \tag{3.6a}$$

$$S_{12} = \frac{b_1}{a_2}\bigg|_{a_1 = 0} \tag{3.6b}$$

$$S_{21} = \frac{b_2}{a_1}\bigg|_{a_2 = 0} \tag{3.6c}$$

$$S_{22} = \frac{b_2}{a_2}\bigg|_{a_1 = 0} \tag{3.6d}$$

where $a_n = 0$ involves no reflection.

S_{11} and S_{22} are the reflection coefficients, S_{12} and S_{21} are the transmission coefficients. The S parameters are complex and are usually expressed in terms of amplitudes and phases, $S_{mn} = |S_{mn}|e^{j\phi_{mn}}$ for m, n = 1, 2. The amplitudes in decibels (dB), are defined as

$$20\log|S_{mn}|dB \qquad m,n = 1,2 \tag{3.7}$$

For filter characterization two parameters are defined, and these are

$$L_A = -20\log|S_{mn}|dB \qquad m,n = 1,2\,(m \neq n) \tag{3.8a}$$

$$L_R = 20\log|S_{nn}|dB \qquad n = 1,2 \tag{3.8b}$$

where L_A is the insertion loss between ports n and m, L_R is the return loss at port n.

When a signal is transmitted through a filter, the output will have a delay in relation with the input, the phase delay (τ_p) and the group delay (τ_d) are related to this delay. The phase delay is the time delay for a steady sinusoidal signal, but it is not the delay of the signal, it is just the delay of the carrier

because a steady sinusoidal signal does not carry information. The true signal delay is represented by the group delay, it is also called the envelope delay. The phase and group delay are defined by

$$\tau_p = \frac{\phi_{21}}{\omega} \text{ seconds} \tag{3.9a}$$

$$\tau_d = -\frac{d\phi_{21}}{d\omega} \text{ seconds} \tag{3.9b}$$

where ϕ_{21} is in radians and ω in radians per second.

The S parameters in terms of the load impedance Z_{01} and the input impedances ($Z_{in1} = V_1/I_1$ $Z_{in2} = V_2/I_2$) are given by

$$S_{11} = \frac{Z_{in1} - Z_{01}}{Z_{in1} + Z_{01}} \tag{3.10a}$$

$$S_{22} = \frac{Z_{in2} - Z_{02}}{Z_{in2} + Z_{02}} \tag{3.10b}$$

A network is said to be symmetrical if $S_{11} = S_{22}$ and is said to be reciprocal if $S_{12} = S_{21}$. For a lossless passive network there is power conservation, i.e., the transmitting power and the reflected power must be equal to the total incident power, the equations for the power conservation are

$$S_{21}S_{21}^* + S_{11}S_{11}^* = 1 \quad or \quad |S_{21}|^2 + |S_{11}|^2 = 1 \tag{3.11a}$$

$$S_{12}S_{12}^* + S_{22}S_{22}^* = 1 \quad or \quad |S_{12}|^2 + |S_{22}|^2 = 1 \tag{3.11b}$$

The transfer function of a two-port filter is a mathematical description of its response characteristics, defined in terms of S_{21}. The amplitude-squared transfer function for a lossless passive filter network is defined as

$$\left|S_{21}(j\Omega)\right|^2 = \frac{1}{1+\varepsilon^2 F_n^2(\Omega)} \tag{3.12}$$

where ε is a ripple constant, $F_n(\Omega)$ is the characteristic function of the filter, and Ω is a frequency variable [30]. It is convenient that Ω represents a radian frequency variable of a lowpass prototype filter with a cutoff frequency at Ω = Ω_c for Ω_c = 1 (rad/s). The insertion loss of the filter for the transfer function described by equation (3.12) is

$$L_A(\Omega) = 10\log\frac{1}{\left|S_{21}(j\Omega)\right|^2}\,dB \tag{3.13}$$

3.3.1 Butterworth filter design

For a Butterworth filter that has an insertion loss L_{Ar} = 3.01 dB at the cutoff frequency Ω_C = 1, a transfer function is given by

$$\left|S_{21}(j\Omega)\right|^2 = \frac{1}{1+\Omega^{2n}} \tag{3.14}$$

where *n* is the degree or the order of filter. This type of response is referred to as maximally flat.

Filter syntheses for realizing the transfer functions result in the so-called lowpass prototype. A lowpass prototype is a filter whose element values are normalized to make the source resistance equal to one, this source resistance is denoted by g_0 = 1 and the cutoff frequency Ω_c = 1(rad/s). Figure 3.13 shows a lowpass prototype where g_i for *i* = 1 to *n* represents the inductance of a series inductor or the capacitance of a shunt capacitor, *n* is the number of reactive elements. These *g*-values are the inductance in Henries, capacitance in Farads, resistance in Ohms, and conductance in mhos. The element values of Figure 3.13 can be obtained from

$$g_0 = 1.0 \tag{3.15a}$$

$$g_i = 2\sin\left(\frac{(2i-1)\pi}{2n}\right) \quad for \quad i = 1 \quad to \quad n \tag{3.15b}$$

$$g_{n+1} = 1.0 \tag{3.15c}$$

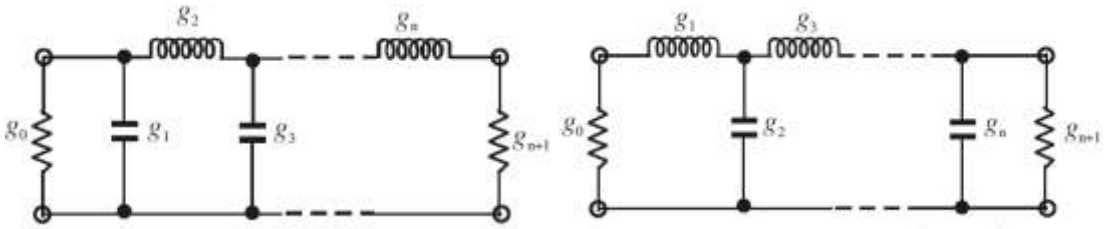

(a) (b)

Figure 3.13. Lowpass prototype filters for all-pole filters with (a) a ladder network structure and (b) its dual [32].

The relation between the external *Q*-factor and the coupling coefficient in terms of *g* values are given below.

$$Q_{e1} = \frac{g_0 g_1}{FBW}, \tag{3.16a}$$

$$Q_{en} = \frac{g_n g_{n+1}}{FBW}, \tag{3.16b}$$

$$M_{i,i+1} = \frac{FBW}{\sqrt{g_i g_{i+1}}}, \tag{3.16c}$$

for i = 1 to n-1,

where Q_{e1} is the input external coupling, Q_{en} is the output external coupling, *FBW* is the fractional bandwidth, and $M_{i,i+1}$ are the internal coupling coefficients.

Figure 3.14 shows a table with calculated element values. For a two-pole filter with fractional bandwidth of 5.5%, the external coupling values and internal coupling values are

$$Q_{e1} = \frac{g_0 g_1}{FBW} = \frac{1.4142}{.055} = 25.71 \tag{3.17a}$$

$$Q_{e2} = \frac{g_2 g_3}{FBW} = \frac{1.4142}{.055} = 25.71 \tag{3.17b}$$

$$M_{1,2} = \frac{FBW}{\sqrt{g_1 g_2}} = \frac{0.055}{\sqrt{(1.4142)(1.4142)}} = 0.0389 \tag{3.17c}$$

n	g_1	g_2	g_3	g_4	g_5	g_6	g_7	g_8	g_9	g_{10}
1	2.0000	1.0								
2	1.4142	1.4142	1.0							
3	1.0000	2.0000	1.0000	1.0						
4	0.7654	1.8478	1.8478	0.7654	1.0					
5	0.6180	1.6180	2.0000	1.6180	0.6180	1.0				
6	0.5176	1.4142	1.9318	1.9318	1.4142	0.5176	1.0			
7	0.4450	1.2470	1.8019	2.0000	1.8019	1.2470	0.4450	1.0		
8	0.3902	1.1111	1.6629	1.9616	1.9616	1.6629	1.1111	0.3902	1.0	
9	0.3473	1.0000	1.5321	1.8794	2.0000	1.8794	1.5321	1.0000	0.3473	1.0

Figure 3.14. Table of element values for Butterworth lowpass prototype filters (g_0 = 1.0, Ω_c = 1, L_{Ar} = 3.01 dB at Ω_c) [32].

3.3.2 Chebyshev filter design

A Chebyshev response exhibits maximally flat stopband and an equal-ripple bandpass, a transfer function that describes these characteristics is given by

$$\left|S_{21}(j\Omega)\right|^2 = \frac{1}{1+\varepsilon^2 T_n^2(\Omega)} \tag{3.18}$$

where, ε, the ripple constant, is related to L_{Ar} by

$$\varepsilon = \sqrt{10^{\frac{L_{Ar}}{10}} - 1} \tag{3.19}$$

and $T_n(\Omega)$ a Chebyshev function of order n and of the first kind, defined as

$$T_n(\Omega) = \begin{cases} \cos(n\cos^{-1}\Omega) & |\Omega| \le 1 \\ \cosh(n\cosh^{-1}\Omega) & |\Omega| \ge 1 \end{cases} \tag{3.20}$$

The filter prototypes shown in Figure 3.13 can also be used for a Chebyshev filter; the element values can be obtained using these equations

$$g_0 = 1.0 \tag{3.21a}$$

$$g_1 = \frac{2}{\gamma}\sin\left(\frac{\pi}{2n}\right) \tag{3.21b}$$

$$g_i = \frac{1}{g_{i-1}} \frac{4\sin\left(\frac{(2i-1)\pi}{2n}\right).\sin\left(\frac{(2i-3)\pi}{2n}\right)}{\gamma^2 + \sin^2\left(\frac{(i-1)\pi}{n}\right)} \qquad for \quad i = 2,3,...,n \tag{3.21c}$$

$$g_{n+1} = \begin{cases} 1.0 & for \quad n \quad odd \\ \coth^2\left(\frac{\beta}{4}\right) & for \quad n \quad even \end{cases} \tag{3.21d}$$

where

$$\gamma = \sinh\left(\frac{\beta}{2n}\right) \tag{3.22a}$$

$$\beta = \ln\left[\coth\left(\frac{L_{Ar}}{17.37}\right)\right] \tag{3.22b}$$

Figure 3.15 shows a table with calculated element values. For a two pole filter with fractional bandwidth of 6.8%, the theoretical external coupling values and theoretical internal coupling value are

$$Q_{e1} = \frac{g_0 g_1}{FBW} = \frac{(1)(0.8431)}{.068} = 12.3985 \quad (3.23a)$$

$$Q_{e2} = \frac{g_2 g_3}{FBW} = \frac{(0.622)(1.3554)}{.068} = 12.3979 \quad (3.23b)$$

$$M_{1,2} = \frac{FBW}{\sqrt{g_1 g_2}} = \frac{0.068}{\sqrt{(0.8431)(0.622)}} = 0.0939 \quad (3.23c)$$

n	g_1	g_2	g_3	g_4	g_5	g_6	g_7	g_8	g_9	g_{10}
1	0.3052	1.0								
2	0.8431	0.6220	1.3554							
3	1.0316	1.1474	1.0316	1.0						
4	1.1088	1.3062	1.7704	0.8181	1.3554					
5	1.1468	1.3712	1.9750	1.3712	1.1468	1.0				
6	1.1681	1.4040	2.0562	1.5171	1.9029	0.8618	1.3554			
7	1.1812	1.4228	2.0967	1.5734	2.0967	1.4228	1.1812	1.0		
8	1.1898	1.4346	2.1199	1.6010	2.1700	1.5641	1.9445	0.8778	1.3554	
9	1.1957	1.4426	2.1346	1.6167	2.2054	1.6167	2.1346	1.4426	1.1957	1.0

Figure 3.15. Table of element values for Chebyshev lowpass prototype filters (g_0 = 1.0, Ω_c = 1, L_{Ar} = 0.1 dB) [32].

3.3.3 Coupling coefficient *k*

A single resonator has a resonance called self-resonance which was presented earlier, when a resonator is close enough to another resonator, there will be a noticeable electromagnetic interaction between them, the self-resonances of the resonators are affected by this interaction, one will be higher than the self-resonance and the other will be lower than the self-resonance, the interaction is measured by the coupling coefficient (*k*). In general, the coupling coefficient of coupled resonators (the resonators can be different in shape and/or size) can be defined by the ratio of coupled energy to stored energy, i.e.,

$$k = \frac{\iiint \varepsilon \underline{E}_1 . \underline{E}_2 d\upsilon}{\sqrt{\iiint \varepsilon |\underline{E}_1|^2 d\upsilon \times \iiint \varepsilon |\underline{E}_2|^2 d\upsilon}} + \frac{\iiint \mu \underline{H}_1 . \underline{H}_2 d\upsilon}{\sqrt{\iiint \mu |\underline{H}_1|^2 d\upsilon \times \iiint \mu |\underline{H}_2|^2 d\upsilon}} \qquad (3.24)$$

where $\underline{E}$ and $\underline{H}$ are the electric and magnetic field vectors, it is more traditional to use k instead of M for the coupling coefficient. Figure 3.16 shows two general coupled resonators. The volume integrals are over all affected regions with permeability μ and permittivity ε. The first term on the right of the equation represents the electric coupling, the second term represents the magnetic coupling. The interaction of the coupled resonators is mathematically described by the dot operation, this allows a positive or negative sign coupling. The direct evaluation of equation (3.24) requires knowledge of the field distributions and performance of the space integrals is a difficult task. It is much easier to use a full-wave EM simulation to find the characteristic frequencies associated to the coupled resonators, If the relationship between the characteristic frequencies and the coupling coefficient is recognized then the coupling coefficient can be determined against the physical structures of the coupled resonators.

The relation between the coupling coefficient and the characteristic frequencies is based on the proximity of the resonators. The extraction of the coupling coefficient of any two coupled resonators can be done by

$$k = \frac{f_2^2 - f_1^2}{f_2^2 + f_1^2}, \qquad (3.25)$$

where f_2 is the highest resonance frequency and f_1 is the lowest resonance frequency [32].

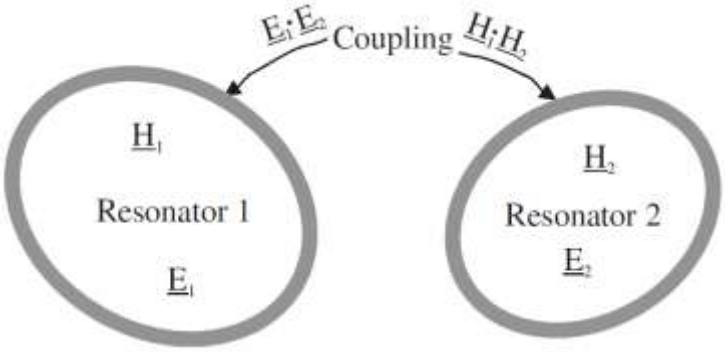

Figure 3.16. General coupled RF/microwave resonators where resonators 1 and 2 can be different in structure and have different resonant frequencies [32].

As mentioned before, the coupling between resonators depends on the proximity of the resonators, a way of controlling the value of k is to move closer or away the resonators. Figure 3.17 shows the circuit layout used to extract the coupling coefficient for the Butterworth filter, where “S” stands for the separation between the resonators; for the Chebyshev filter the same layout is used except that the square ring has a gap at 90°. Figure 3.18 shows the relation between the coupling coefficients and the separation between resonators. The interaction between resonators is larger when the resonators are closer.

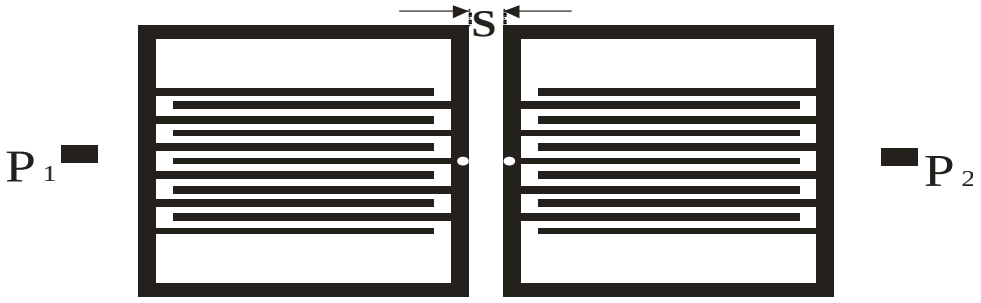

Figure 3.17. Circuit layout used to extract the coupling coefficient for the Butterworth filter.

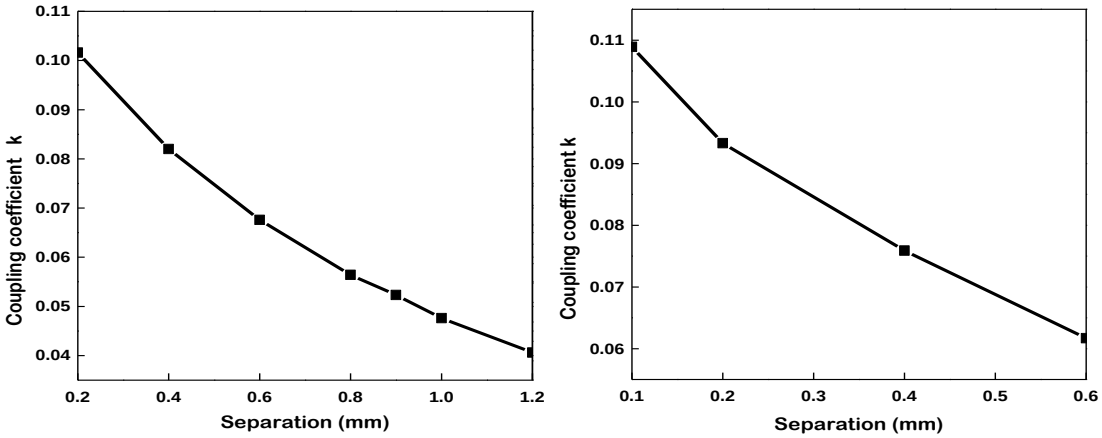

(a) (b)

Figure 3.18. Relation between separation and coupling coefficient for (a) Butterworth filter and (b) Chebyshev filter.

3.3.4 External coupling Q_e

For symmetrical resonators the equivalent circuit is a two-port network as shown in Figure 3.19, the symmetrical plane is represented by $T-T'$, the *LC* resonators have been separated into two parts. When the symmetrical plane $T-T'$ is a short-circuit, the following equation can be obtained

$$Y_{ino} = \infty , \tag{3.26a}$$

$$S_{11o} = \frac{G - Y_{ino}}{G + Y_{ino}} = -1 \tag{3.26b}$$

where S_{11o} and Y_{ino} are the odd-mode reflection coefficient at port 1 and the input admittance. When the $T-T'$ plane is replaced by an open circuit, the following equations are obtained for the even mode

$$Y_{ine} = j\omega_0 C\Delta\omega/\omega_0 , \tag{3.27a}$$

$$S_{11e} = \frac{G - Y_{ine}}{G + Y_{ine}} = \frac{1 - jQ_e\Delta\omega/\omega_0}{1 + jQ_e\Delta\omega/\omega_0} \tag{3.27b}$$

where $\omega_0 = 1/\sqrt{LC}$ and $(\omega^2 - \omega_0^2)/\omega \approx 2\Delta\omega$ when $\omega = \omega_0 + \Delta\omega$ has been used

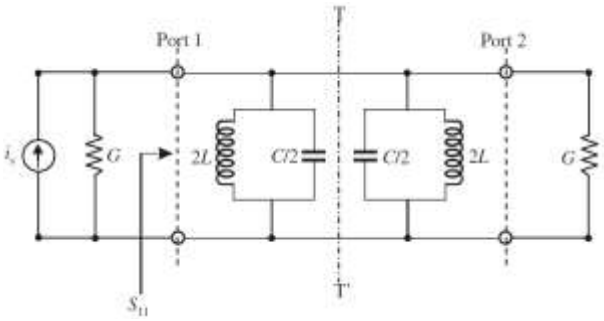

Figure 3.19. Equivalent circuit of the I/O resonator with double loading [32].

Using the equivalence $S_{21} = ½(S_{11e} - S_{11o})$ then S_{21} can be expressed as

$$S_{21} = \frac{1}{1 + jQ_e\Delta\omega/\omega_0} \tag{3.28a}$$

$$|S_{21}| = \frac{1}{\sqrt{1 + (Q_e\Delta\omega/\omega_0)^2}} \tag{3.28b}$$

The graph of equation (3.28b) is shown in Figure 3.20. The function has its maximum value when $\Delta\omega = 0$ and the value is 1, when

$$Q_e \frac{\Delta\omega_{\pm}}{\omega_0} = \pm 1 \tag{3.29}$$

the value of $|S_{21}|$ is 0.707 (-3 dB). From the definition of the bandwidth, the following equation is obtained

$$\Delta\omega_{3dB} = \Delta\omega_{+} - \Delta\omega_{-} = \frac{\omega_0}{Q_e/2} \tag{3.30}$$

From the above equation, the external quality factor Q_e is

$$Q_e' = \frac{Q_e}{2} = \frac{\omega_0}{\Delta\omega_{3dB}} \tag{3.31}$$

where ω_0 is the central frequency and $\Delta\omega_{3dB}$ is the difference between the high and low frequency values that are 3 dB below the central frequency value, Q_e is the single loaded external quality factor, and Q'_e is the double loaded external quality factor.

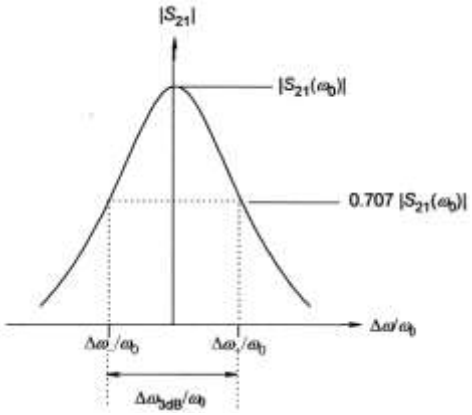

Figure 3.20. Resonant amplitude response of S_{21} for the circuit shown in Figure 3.19 [32]

The two typical input/output coupling structures for coupled microstrip resonator filters are the tapped line and the coupled line structures. For the tapped line a 50 ohm microstrip feed line is directly tapped onto the input or/and output of the resonator. For the coupled line, the coupling is obtained by the proximity of the structure and the feeding line, Figure 3.21(a) shows the coupled line structure used for the Butterworth filter, the gap amid the ring and the feeding line is denoted by *g*, the coupling will decrease as *g* increases, another way of reducing and controlling the coupling is the reduction in the length of the line denoted as "R" on the circuit. From this point on the external coupling is denoted by Q_e. Figure 3.21(b) shows the relation between Q_e values and the reduction of the horizontal lines R. The external coupling for the Chebyshev filter was done using the tapped line, which is shown in Figure 3.22(a), Figure 3.22(b) shows the relation between the external coupling and the distance "D", where D is the distance from the edge to the feeding line tapped to the resonator.

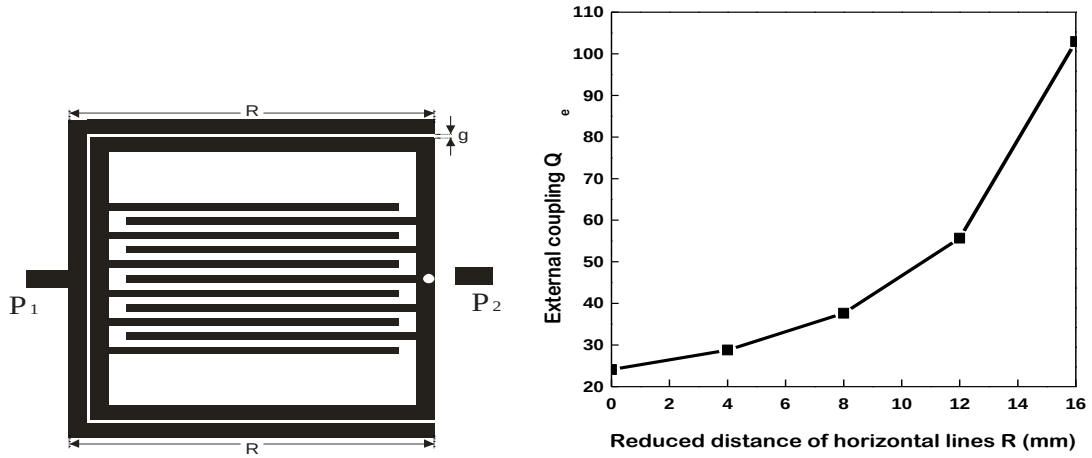

(a) (b)

Figure 3.21. (a) Circuit layout used to obtain the external coupling Q_e. (b) Relation between Q_e and R for the Butterworth filter.

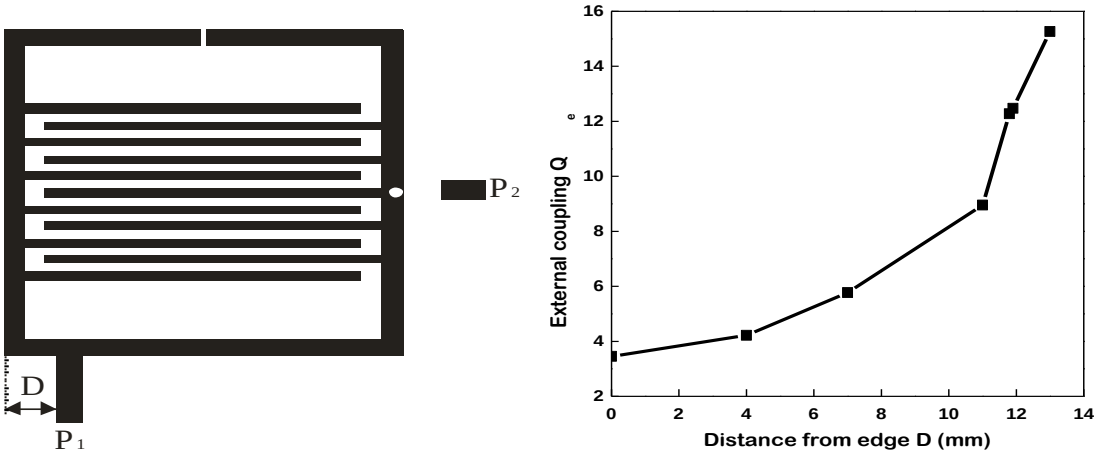

(a) (b)

Figure 3.22. (a) Circuit layout used to obtain the external coupling Q_e. (b) Relation between Q_e and D for the Chebyshev filter.

3.4 Results and Discussion

To confirm and demonstrate the frequency response of the novel square ring resonator with a via to ground and an interdigital capacitor discussed earlier, two kinds of filters are simulated using a full-wave EM simulator [29]. A

substrate with ε_r = 10.8 and a thickness of 1.27 mm is used (Rogers Duroid 6010). For the requirement of 50 Ω impedance, the width of the microstrip is 1.0 mm, the effective dielectric constant is ε_{eff} = 7. The dimensions of the resonator are: external square ring perimeter 62.4 mm, internal square ring perimeter 59.2 mm, capacitor-finger length 13.2 mm, capacitor-finger width 0.4 mm, separation between fingers 0.4 mm, and via to ground diameter 0.5 mm. For the Butterworth filter, a coupled line structure is implemented, the dimensions of the coupled line surrounding the resonators are: width of the line 0.8 mm, length of the line 49.2 mm, separation between coupled line and resonator 0.2 mm. The total dimensions of the Butterworth filter without connectors and feed lines are: 34.4 x 17.6 mm^2. For the Chebyshev filter, the same resonator is used except that it is an open square ring with an aperture of 0.2 mm. A tapped line is used for the excitation. The total dimensions of the Chebyshev filter without connectors and feed lines are: 31.4 x 15.6 mm^2. For both filters, the dimensions of the feeding lines are: line width= 1.0 mm and line length=4.0 mm. The proposed circuits were fabricated using a serigraphy process. Photographs of the fabricated circuits are shown in Figure 3.23. Measurements were performed using the Agilent PNA series microwave vector network analyzer (E8361A) to determine the filter performances. Simulated and measured reflection and transmission coefficient responses of the proposed filters are shown in Figure 3.24 and 3.25, respectively. From these figures, it is evident that the simulation and measured frequency responses are in good agreement. Table 3.1 presents the simulated and fabricated filter characteristics of the Butterworth and Chebyshev filters. For the Butterworth filter, there is an insertion loss of 2.3 dB and a return loss of 25 dB at the central frequency. For the Chebyshev filter, there is an insertion loss of 2.2 dB and a return loss of 12.64 dB at the central frequency. The differences between simulated and measured values of the filters may be due to the fabrication errors.

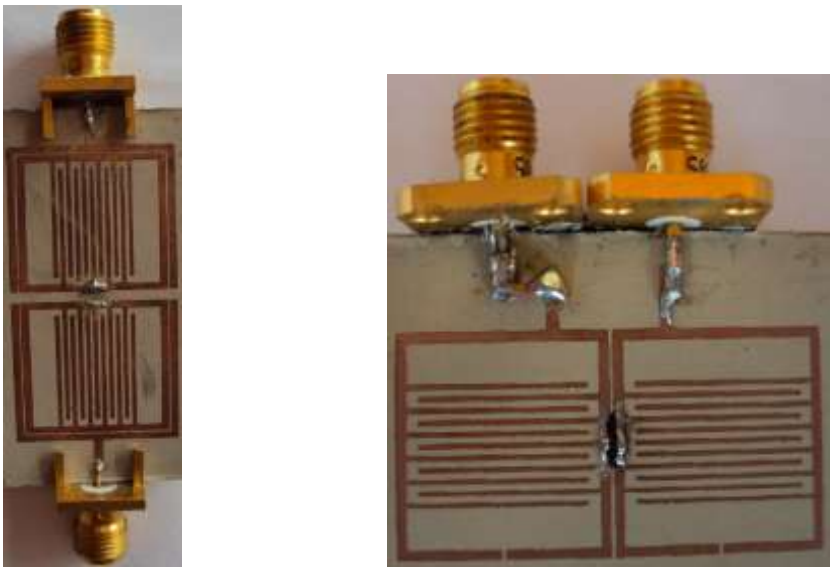

(a) (b)

Figure 3.23. Photographs of the fabricated circuits (a) Butterworth filter and (b) Chebyshev filter.

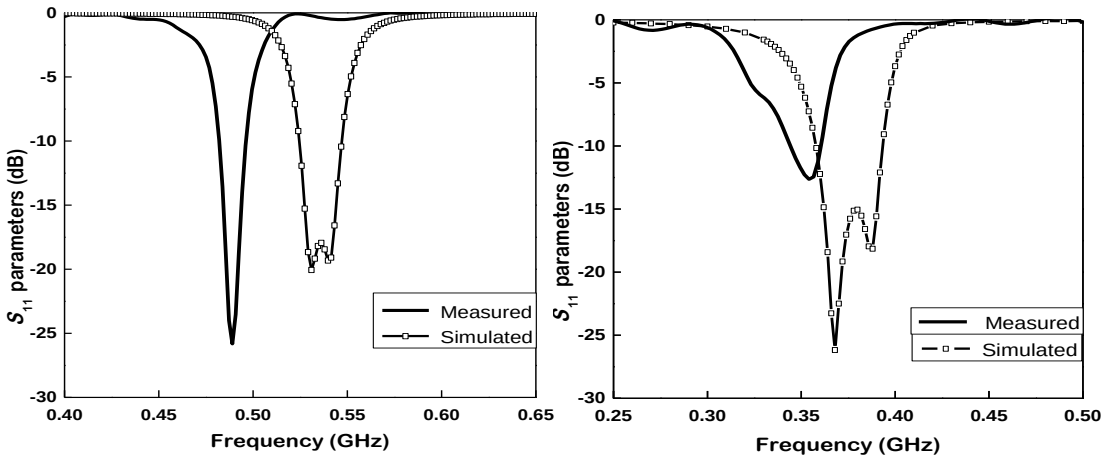

a) b)

Figure 3.24. Measured and simulated S_{11} parameters of (a) Butterworth filter and (b) Chebyshev filter.

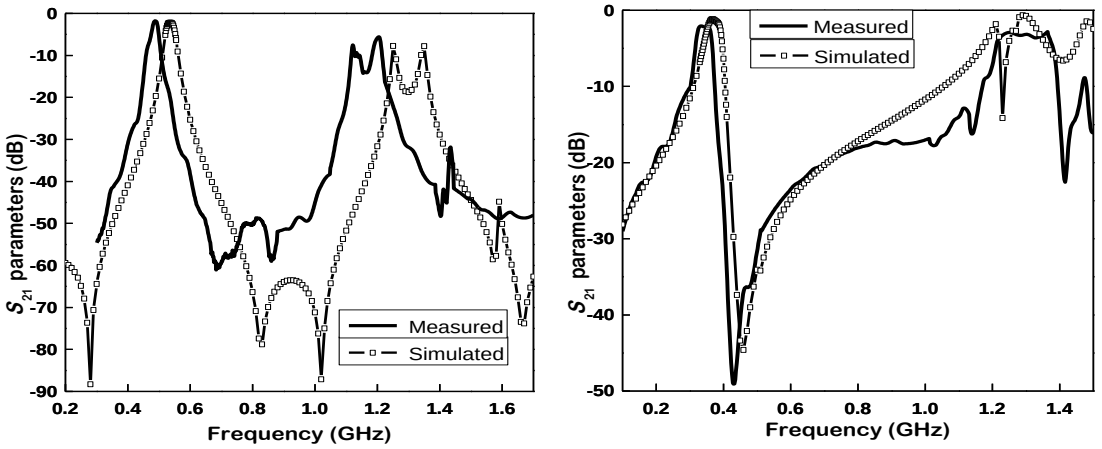

Figure 3.25. Measured and simulated S_{21} parameters of (a) Butterworth filter and (b) Chebyshev filter.

Table 3.1. Comparison between simulated and measured values of the Butterworth and Chebyshev filters.

	Butterworth		**Chebyshev**	
	Simulated	Measured	Simulated	Measured
Central frequency (GHz)	0.531	0.489	0.38	0.354
Insertion loss (dB)	2.23	2.3	1.51	2.2
Return loss (dB)	18	25	15.05	12.64
Fractional bandwidth %	6.1	5	14.6	14.4

Chapter IV

Quasi elliptic filter

In this chapter a Quasi-elliptic filter based on the square ring resonator with a via to ground and an interdigital capacitor is presented. The basic theory about electric, magnetic and mixed coupling which is important for the design of Quasi-elliptic filters is offered. Design procedure, simulation and measured results of the quasi-elliptic filter are explained in detail.

4.1 Coupled resonators

The general theory of coupling was mentioned in the earlier chapter, for just one internal coupling the general theory is good enough, but for some applications a better developed technique is required. Figure 4.1 shows the two-port network for an *n*-coupled resonator, the *EM* resonators can have electric coupling, magnetic coupling or mixed coupling. The next subsections present the main characteristics of these couplings.

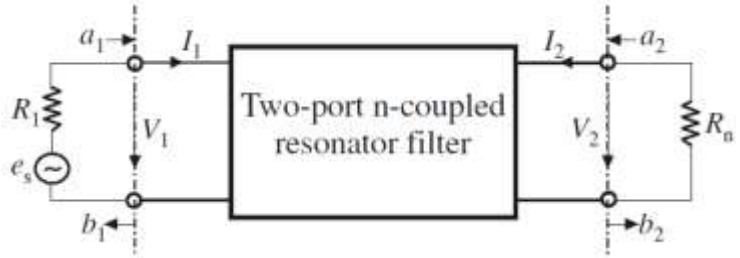

Figure 4.1. Network representation of *n*-coupled resonators [32].

4.1.1 Electric coupling

A circuit model using lumped elements for electrically coupled resonators is shown in Figure 4.2(a); *L* is the self-inductance, *C* is the self-capacitance, C_m stands for the mutual capacitance, and the resonant frequency of uncoupled resonators is $(LC)^{-1/2}$. If the elements are not lumped but distributed, this equivalent circuit is just valid for the frequencies near the resonance. The planes $T_1 - T_1'$ and $T_2 - T_2'$ divide the circuit and taking the circuit between those two planes a two-port network is obtained. The equations for the two-port network are

$$I_1 = j\omega C V_1 - j\omega C_m V_2 \tag{4.1a}$$

$$I_2 = j\omega C V_2 - j\omega C_m V_1 \tag{4.1b}$$

The *Y* parameters for the two-port network are

$$Y_{11} = Y_{22} = j\omega C \tag{4.2a}$$

$$Y_{12} = Y_{21} = -j\omega C_m \tag{4.2b}$$

An alternative form of the circuit in Figure 4.2(a) is shown in Figure 4.2(b). The electric coupling between two loop resonators is characterized by an admittance inverter $J = \omega C_m$. If an electric wall (short circuit) is placed instead of the symmetry plane $T - T'$, the resonant frequency of the resultant circuit is

$$f_e = \frac{1}{2\pi\sqrt{L(C + C_m)}} \tag{4.3}$$

Equally, if a magnetic wall (open circuit) is placed instead of the symmetry plane $T - T'$, the resonant frequency of the resultant circuit is

$$f_m = \frac{1}{2\pi\sqrt{L(C - C_m)}} \tag{4.4}$$

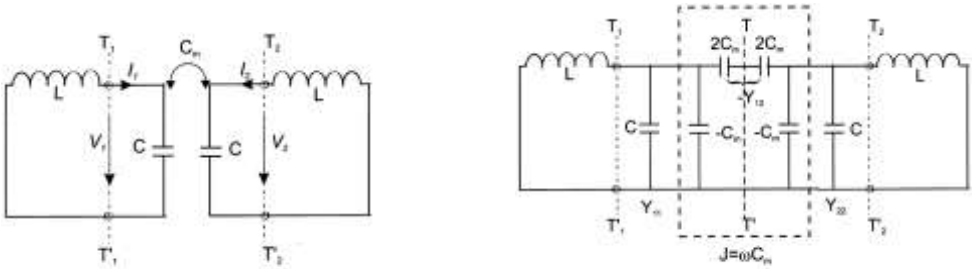

(a) (b)

Figure 4.2. (a) Synchronously tuned coupled resonator circuit with electric coupling. (b) Alternative form of the equivalent circuit with an admittance inverter $J = \omega C_m$ to represent the coupling [32].

For the electric wall the frequency is lower than the one associated frequency for an uncoupled single resonator, the capability for storing charge is enhanced by the coupling effect. For the magnetic wall the inverse circumstances occur. Using the two resonance frequencies the electric coupling coefficient can be found

$$k_E = \frac{f_m^2 - f_e^2}{f_m^2 + f_e^2} = \frac{C_m}{C} \tag{4.5}$$

4.1.2 Magnetic coupling

Similarly, a circuit model using lumped elements for magnetically coupled resonators is shown in Figure 4.3(a), *L* is the self-inductance, *C* is the self-capacitance, L_m stands for the mutual inductance. Again the planes $T_1 - T_1'$ and $T_2 - T_2'$ divide the circuit and the equations for the two-port network are

$$V_1 = j\omega L I_1 + j\omega L_m I_2 \tag{4.6a}$$

$$V_2 = j\omega L I_2 + j\omega L_m I_1 \tag{4.6b}$$

The *Z* parameters for this two-port network are

$$Z_{11} = Z_{22} = j\omega L \tag{4.7a}$$

$$Z_{12} = Z_{21} = -j\omega L_m \tag{4.7b}$$

Figure 4.3(b) shows an equivalent circuit for the coupled resonator. The magnetic coupling between two loop resonators is characterized by an impedance inverter $K = \omega L_m$, when an electric wall (short circuit) is placed instead of the symmetry plane $T - T'$ in Figure 4.3(b). The resonant frequency of the resultant circuit is

$$f_e = \frac{1}{2\pi\sqrt{C(L - L_m)}} \tag{4.8}$$

Likewise, if a magnetic wall (open circuit) is placed instead of the symmetry plane $T - T'$, the resultant resonant frequency is

$$f_m = \frac{1}{2\pi\sqrt{C(L + L_m)}} \tag{4.9}$$

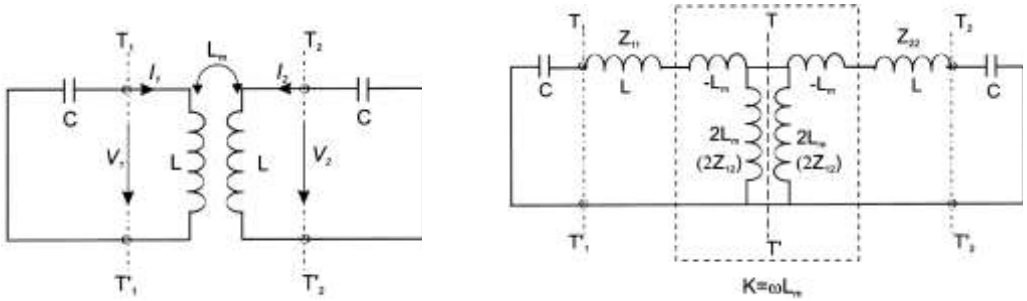

(a) (b)

Figure 4.3. (a) Synchronously tuned coupled resonator circuit with magnetic coupling. (b) Alternative form of the equivalent circuit with an impedance inverter $K = \omega L_m$ to represent the coupling [32].

For the electric wall the frequency is higher because the stored flux is reduced by the coupling effect. For the magnetic wall the stored flux is increased and the resonance frequency is lower. In the same way, the magnetic coupling coefficient can be found using the electric and magnetic resonances

$$k_M = \frac{f_e^2 - f_m^2}{f_e^2 + f_m^2} = \frac{L_m}{L} \tag{4.10}$$

4.1.3 Mixed coupling

Figure 4.4(a) presents a network representation for structures with electric and magnetic couplings. The *Y* and *Z* parameters are

$$Y_{11} = Y_{22} = j\omega C \tag{4.11a}$$

$$Y_{12} = Y_{21} = j\omega C_m \tag{4.11b}$$

$$Z_{11} = Z_{22} = j\omega L \tag{4.11c}$$

$$Z_{12} = Z_{21} = j\omega L_m \tag{4.11d}$$

where C is the self-capacitance, L is the self-inductance, C_m is the mutual capacitance, and L_m is the mutual inductance of the associated circuit shown in Figure 4.4(b) with equivalent lumped-elements. The electric coupling is represented with an admittance inverter $J = \omega C_m$, the magnetic coupling is represented with an impedance inverter $K = \omega L_m$.

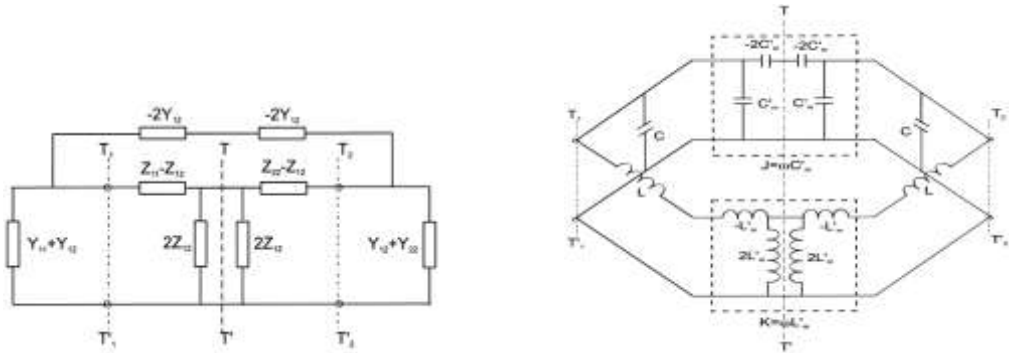

(a) (b)

Figure 4.4. (a) Network representation of synchronously tuned coupled resonator circuit with mixed coupling. (b) An associated equivalent circuit with an impedance inverter *K* and an admittance inverter *J* to represent the magnetic and electric coupling, respectively [32].

The same procedure is applied to mixed coupling, by placing an electric wall and a magnetic wall where the symmetry plane $T-T'$ is, the next associated frequencies are obtained

$$f_e = \frac{1}{2\pi\sqrt{(L-L_m)(C-C_m)}} \tag{4.12a}$$

$$f_m = \frac{1}{2\pi\sqrt{(L+L_m)(C+C_m)}} \tag{4.12b}$$

Based on those two frequencies the mixed coupling coefficient is

$$k_X = \frac{f_e^2 - f_m^2}{f_e^2 + f_m^2} = \frac{CL_m + LC_m}{LC + L_m C_m} \tag{4.13}$$

$L_m < L$ and $C_m < C$, so that $L_m C_m << LC$ and (4.13) can be reduced to

$$k_X \approx \frac{L_m}{L} + \frac{C_m}{C} = k_M + k_E \tag{4.14}$$

As can be seen, the magnetic and mixed coupling coefficients have similar equations, and both of them are opposite in sign to the electric coefficient coupling. In general, if the electric frequency resonance is placed first on the right part of the coefficient coupling equations we have

$$k_E = \frac{f_m^2 - f_e^2}{f_m^2 + f_e^2} = -\frac{f_e^2 - f_m^2}{f_e^2 + f_m^2} \tag{4.15}$$

The electric coupling coefficient is said to be negative, as can be seen on equation (4.15). The mixed coupling is a superposition of the electric and magnetic coupling. The electric and magnetic coupling can have two opposite effects, and these effects can cancel or enhance each other.

4.2 Opposite phases

The use of the above formulas can be clarified with the typical types of coupled microstrip resonators as depicted in Figure 4.5. All the resonators are open-loop resonators, each resonator has the maximum electric field density at the side with an open gap and the maximum magnetic field density at the opposite side. Figure 4.5(a) shows the arrangement for electric coupling. Figure 4.5 (b) depicts the arrangement for the magnetic coupling. The typical mixed coupling arrangements are shown in Figure 4.5(c) and (d). Usually, the magnitude of the magnetic coupling is larger than the magnitude of the electric coupling for the same proximity between the rings. As mentioned before, for the mixed coupling, the electric and magnetic coupling can enhance or annul each other depending on the distribution of the fields. For the arrangements shown in Figure 4.5(d) the magnetic and electric couplings will enhance and annul each other depending of the separation between the resonators. It has been mentioned that the magnetic coupling and the electric coupling have opposite signs; one way of proving it is by comparing their phases, if they are out of phase then the signs of the magnetic and electric coupling must be opposite. When comparing the phases, the locations of the ports with respect to the coupled resonators must be the same for both arrangements. Figure 4.6 shows the phases for the electric and magnetic coupling arrangement. By comparing the phases, it can be observed that both are out of phase. This is evidence that the two coupling coefficients have opposite signs.

The above mentioned procedure is used for the design of a Quasi-elliptic filter with the close square ring resonator with via to ground and interdigital capacitor. When the via is placed on one side, it has the maximum magnetic field density and the opposite side has the maximum electric field density.

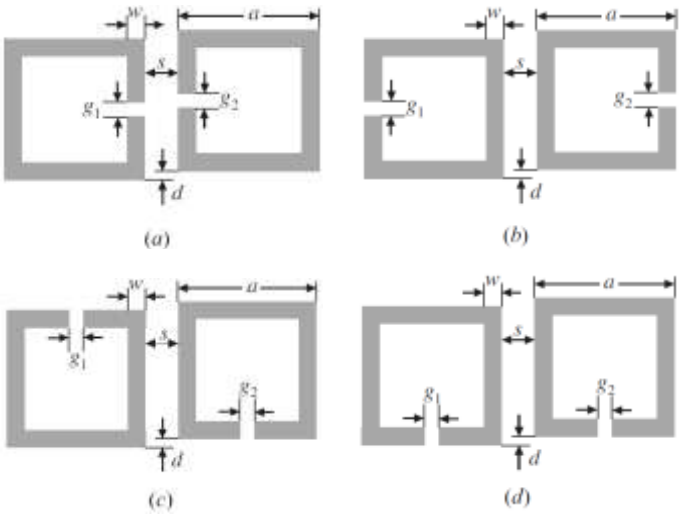

Figure 4.5. Typical coupling structures of coupled resonators with (a) electric coupling, (b) magnetic coupling, (c) and (d) mixed coupling [32].

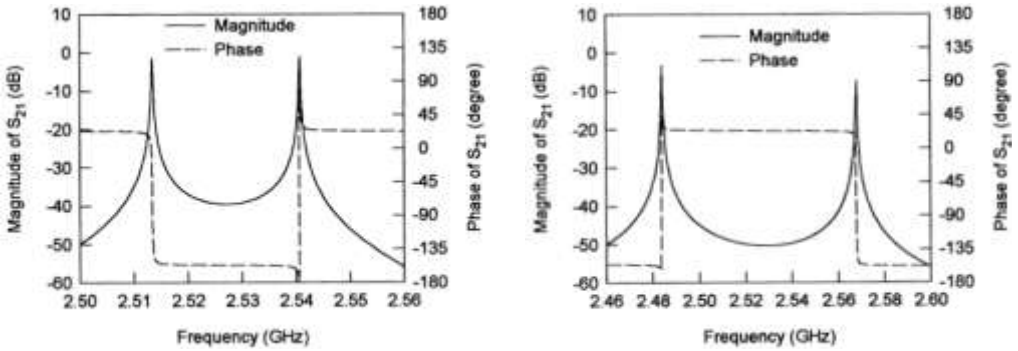

Figure 4.6. Typical resonant responses of coupled resonator structures. (a) For the structure in Figure 4.5(a). (b) For the structure in Figure 4.5(b) [32].

Figure 4.7 shows the arrangement of an electric coupling for the close square ring resonator with a via to ground and an interdigital capacitor and the response of the electric coupling. Figure 4.8 shows the magnetic coupling arrangement and its response. Figure 4.9 shows the arrangement of the mixed coupling. As can be seen, the electric and magnetic arrangement responses are out of phase, which implies that their corresponding couplings have opposite sign. The opposite sign represents an extra advantage for a resonator because the resonator can be used to implement a Quasi-elliptic filter.

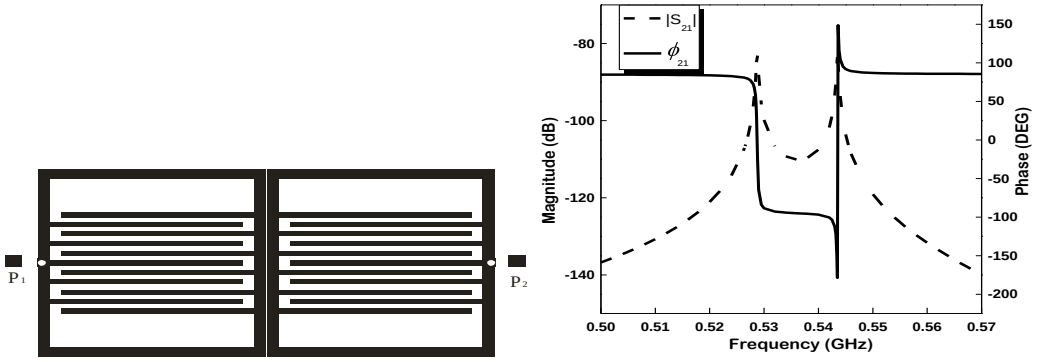

(a) (b)

Figure 4.7. (a) Circuit layout of electric coupling. (b) $|S_{21}|_{dB}$ and ϕ_{21}°.

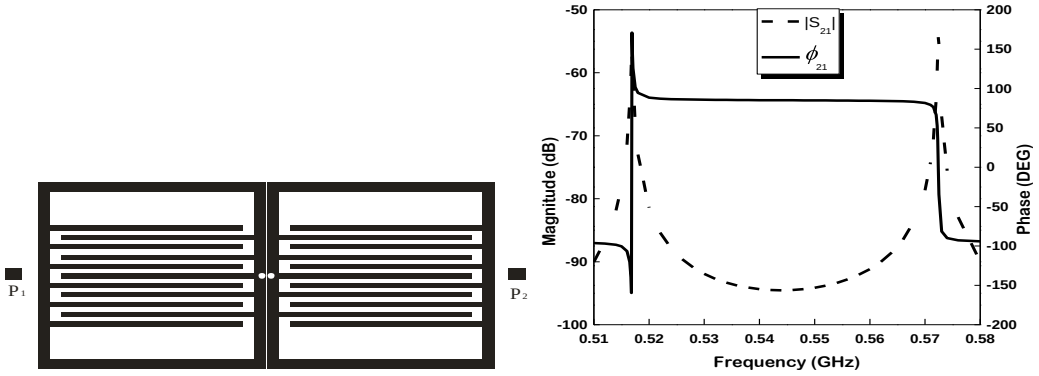

(a) (b)

Figure 4.8. (a) Circuit layout of magnetic coupling. (b) $|S_{21}|_{dB}$ and ϕ_{21}°.

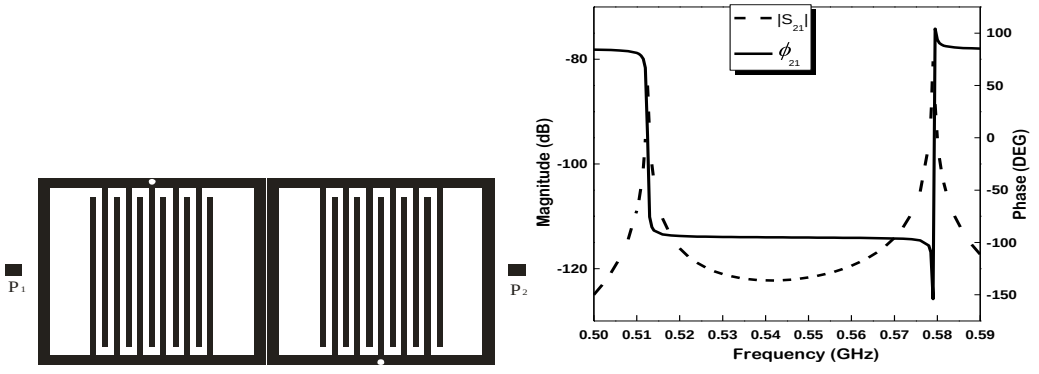

(a) (b)

Figure 4.9. (a) Circuit layout of mixed coupling. (b) $|S_{21}|_{dB}$ and ϕ_{21}°.

4.3 Design of a Quasi-elliptic filter

In [33] a filter having two transmission zeros (attenuation poles) at finite frequencies is presented. This filter shows an improvement on skirt selectivity and the characteristics of this filter are between a Chebyshev and an elliptic filter. The filter characteristics are not as good as the ones of an elliptic filter but its physical realization is easier than the elliptic one. The transfer function for this kind of filter is

$$\left|S_{21}(\Omega)\right|^2 = \frac{1}{1+\varepsilon^2 F_n^2(\Omega)} \tag{4.16a}$$

$$\varepsilon = \frac{1}{\sqrt{10^{-\frac{L_R}{10}} - 1}} \tag{4.16b}$$

$$F_n(\Omega) = \cosh\left\{(n-2)\cosh^{-1}(\Omega) + \cosh^{-1}\left(\frac{\Omega_a\Omega - 1}{\Omega_a - \Omega}\right) + \cosh^{-1}\left(\frac{\Omega_a\Omega + 1}{\Omega_a + \Omega}\right)\right\} \tag{4.16c}$$

where ε is a ripple constant that is related to a return loss $L_R = 20\log|S_{11}|_{dB}$, n is the filter degree, and Ω is the normalized frequency variable. $\Omega = \pm\Omega_a$ (Ω_a>1) are the locations of the transmission zeros on the frequency chart. As $\Omega_a \rightarrow \infty$ the filtering function $F_n(\Omega)$ becomes the Chebyshev function. The two finite frequency transmission zeros location of a bandpass filter are

$$\omega_{a1} = \omega_0 \frac{-\Omega_a FBW + \sqrt{(\Omega_a FBW)^2 + 4}}{2} \tag{4.17a}$$

$$\omega_{a2} = \omega_0 \frac{\Omega_a FBW + \sqrt{(\Omega_a FBW)^2 + 4}}{2} \tag{4.17b}$$

where *FBW* is the fractional bandwidth

Figure 4.10 presents the typical responses of a four-pole filter with L_R = -20 dB. The responses are compared with a Chebyshev filter; as shown, there is a higher selectivity for values of Ω closer to 1. In [34] a method based on a lowpass prototype filter is developed, where rectangular boxes represent ideal admittance inverters (J_s) and the capacitors represent admittances (g_s). From this lowpass prototype filter bandpass filters have been designed. Figure 4.11 shows the prototype, the g_s are the element values for Chebyshev filters.

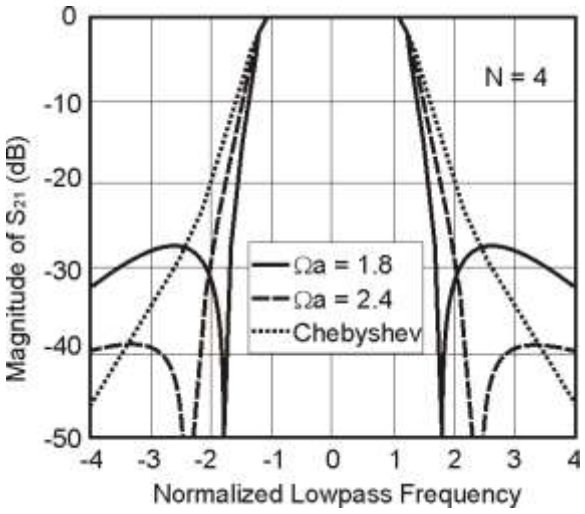

Figure 4.10. Comparison of frequency responses of the Chebyshev filter and the filter with a single pair of attenuation poles at finite frequencies (n = 4) [33].

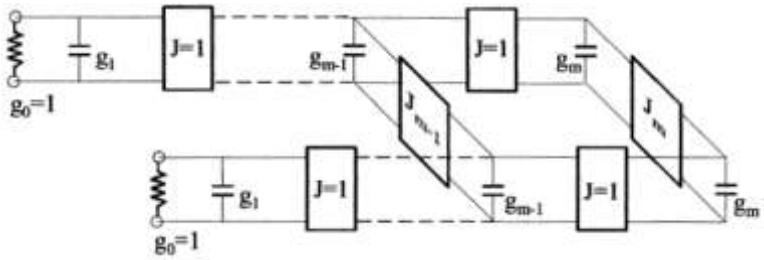

Figure 4.11. Lowpass prototype filter for the filter synthesis [32].

The authors in [33] developed formulas by curve fitting for obtaining the values of the admittance inverters and the element values, these formulas are

$$g_1(\Omega_a) = 1.22147 - 0.35543\Omega_a + 0.18337\Omega_a^2 - 0.0447\Omega_a^3 + 0.00425\Omega_a^4 \quad (4.18a)$$

$$g_2(\Omega_a) = 7.22106 - 9.48678\Omega_a + 5.89032\Omega_a^2 - 1.65776\Omega_a^3 + 0.17723\Omega_a^4 \quad (4.18b)$$

$$J_1(\Omega_a) = -4.30192 + 6.26745\Omega_a - 3.67345\Omega_a^2 + 0.9936\Omega_a^3 - 0.10317\Omega_a^4 \quad (4.18c)$$

$$J_2(\Omega_a) = 8.17573 - 11.36315\Omega_a + 6.96223\Omega_a^2 - 1.94244\Omega_a^3 + 0.20636\Omega_a^4 \quad (4.18d)$$

($n = 4$ and $1.8 \le \Omega_a \le 2.4$)

For a four-pole filter (*m* = 2) these equations are related to the coupling coefficients and external quality factors by

$$Q_{ei} = Q_{eo} = \frac{g_1}{FBW} \quad (4.19a)$$

$$M_{1,2} = M_{3,4} = \frac{FBW}{\sqrt{g_1 g_2}} \quad (4.19b)$$

$$M_{2,3} = \frac{FBW.J_2}{g_2} \quad (4.19c)$$

$$M_{1,4} = \frac{FBW.J_1}{g_1} \quad (4.19d)$$

The general coupling structure for a bandpass filter is shown in Figure 4.12(a). Figure 4.12(b) shows the configuration of the filter using open square ring resonators. For Ω_a = 1.8 and a bandpass filter with a fractional bandwidth of 10%, the following values are obtained

$$g_1(1.8) = 0.95974 \quad (4.20a)$$

$$g_2(1.8) = 1.42192 \quad (4.20b)$$

$$J_1(1.8) = -0.21083 \quad (4.20c)$$

$$J_2(1.8) = 1.11769 \tag{4.20d}$$

$$Q_{ei} = Q_{eo} = \frac{0.95974}{0.1} = 9.5974 \tag{4.20e}$$

$$M_{1,2} = M_{3,4} = \frac{0.1}{\sqrt{(0.95974)(1.42192)}} = 0.0856 \tag{4.20f}$$

$$M_{2,3} = \frac{(0.1)(1.11769)}{1.42192} = 0.0786 \tag{4.20g}$$

$$M_{1,4} = \frac{(0.1)(-0.21083)}{0.95974} = -0.02196 \tag{4.20h}$$

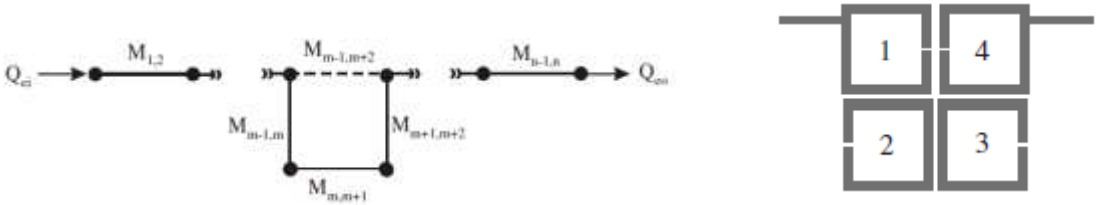

(a) (b)

Figure 4.12. (a) General coupling structure of the bandpass filter with a single pair of finite-frequency zeros. (b) Configuration of microstrip bandpass filter [32].

4.3.1 Coupling coefficients $M_{1,4}$, $M_{2,3}$, $M_{3,4}$, and $M_{1,2}$

The detailed extraction procedure of coupling coefficient values is discussed in the earlier chapter. Figure 4.7(a) and 4.8(a) show the circuit layouts used for the evaluation of the coupling coefficients $M_{1,4}$ and $M_{2,3}$ respectively. The relation between the coupling coefficient $M_{1,4}$ with the separation of the resonators and coupling coefficient $M_{2,3}$ with the separation of the resonators is presented in Figure 4.13(a) and (b) respectively. Finally, the extraction of the coupling coefficients $M_{3,4}$ and $M_{1,2}$ is done using the circuit layout shown in

Figure 4.9(a). The relation between the coupling coefficient $M_{3,4}$ and $M_{1,2}$ *with* the separation of the resonators is shown in Figure 4.14. The desired coupling coefficient values are selected from the depicted graphs.

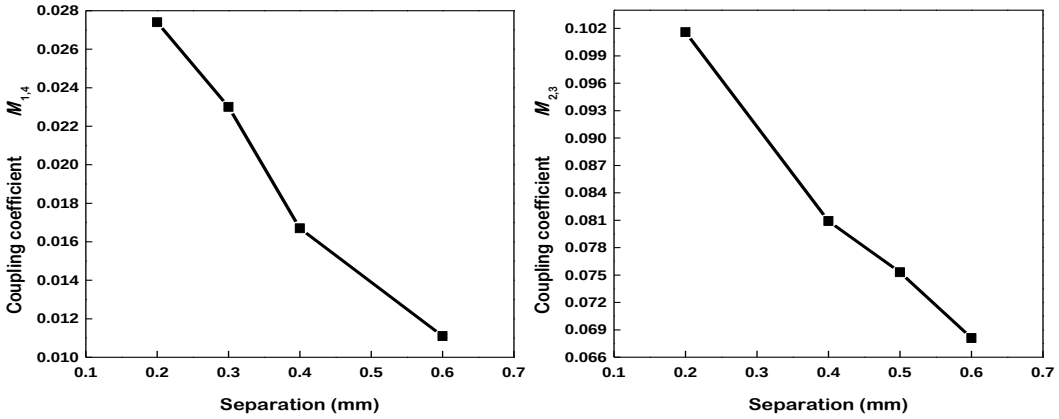

(a) (b)

Figure 4.13. Relation between separation and coupling coefficients (a) $M_{1,4}$ and (b) $M_{2,3}$.

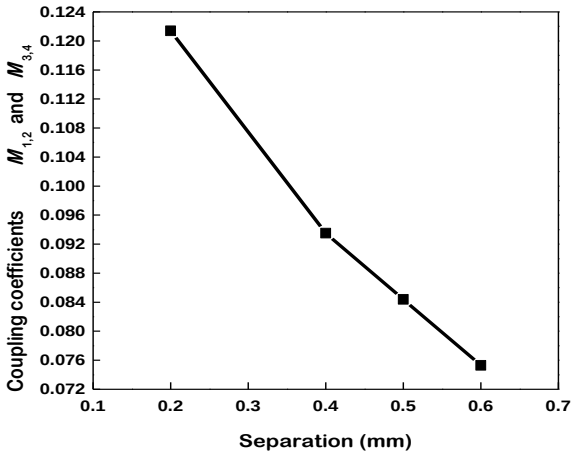

Figure 4.14. Relation between separation and coupling coefficients $M_{1,2}$ and $M_{3,4}$.

4.3.2 External couplings Q_{ei} and Q_{eo}

The circuit layout used for extracting the external couplings is shown in Figure 4.15(a). Simulations were performed to obtain the external couplings by

moving the position of the tapped line with respect to the corner of the close square ring resonator. “D” represents the distance from the corner of the resonator to the tapped line as shown in Figure 4.15(a). Figure 4.15(b) shows the relation between the external couplings and the distance of the left-edge tapped line. The desired external coupling values are chosen from the depicted graph.

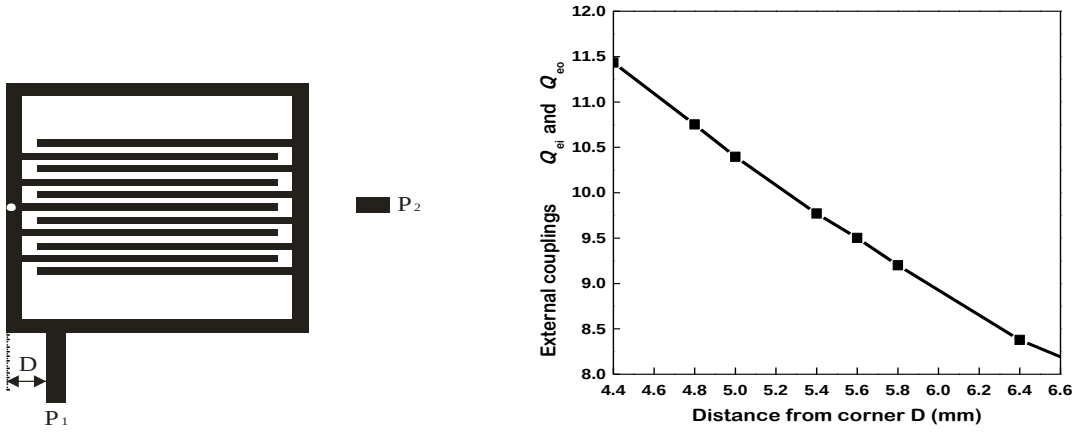

(a) (b)

Figure 4.15. (a) Layout of circuit for obtaining the external coupling values. (b) Relation between the external couplings (Q_{ei} and Q_{eo}) and D.

4.4 Results and Discussion

The filter is realized using the configuration of Figure 4.12(b). It is fabricated using the serigraphy process. RT/Duroid substrate with a relative dielectric constant of 10.8 and a thickness of 1.27 mm is chosen for its implementation. Figure 4.16 is a photograph of the fabricated filter. The size of the filter without connectors is 35.7 x 31.7mm^2. The feeding is by 50 Ω microstrip lines of 1.0 mm width and 4.0 mm length. Measurements are performed using the Agilent PNA series microwave vector network analyzer (E8361A). Figure 4.17 shows the simulated and measured reflection and transmission coefficient of the filter. The mid-band insertion loss is about 1.3 dB, which is attributed to the conductor loss of copper and the return loss at central frequency is 13.81 dB. The two attenuation poles near the cutoff frequencies of the bandpass are

observable, which improve the selectivity. The differences between simulated and measured values are attributed to the fabrication process, as can be seen from the photograph, capacitor-finger lines are not identical and as a consequence, the associate resonance of the resonators may be different. Table 4.1 presents the simulated and fabricated main filter characteristics for the Quasi-elliptic filter.

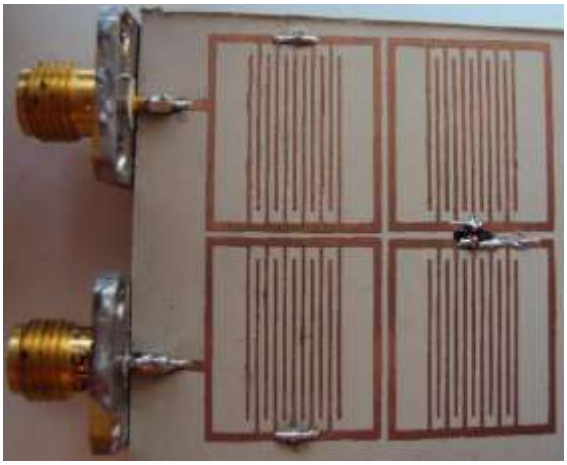

Figure 4.16. Photograph of the fabricated Quasi-elliptic filter.

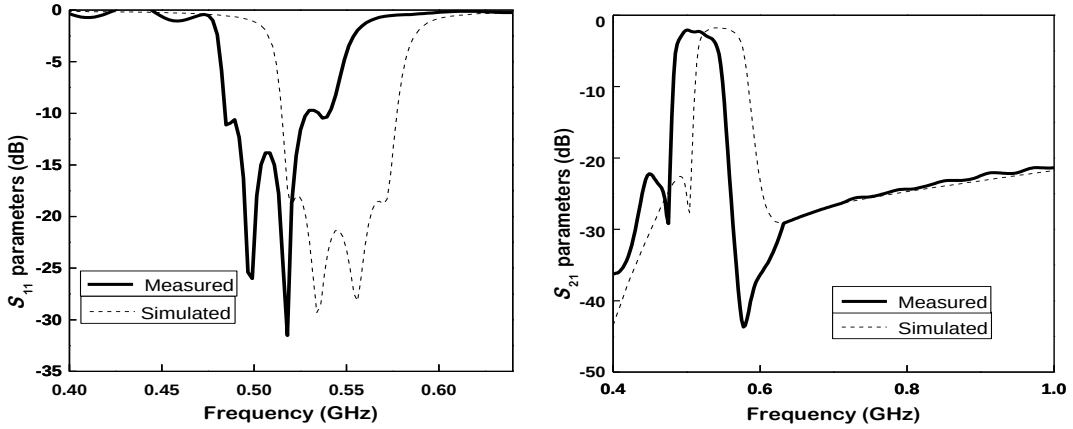

(a) (b)

Figure 4.17. Measured and simulated *S* parameters (a) S_{11} and (b) S_{21}.

Table 4.1. Comparison between simulated and measured values of the Quasi-elliptic filter.

	Simulated	Measured
Central frequency (GHz)	0.546	0.506
Insertion loss (dB)	1.77	1.88
Return loss (dB)	21.35	13.81
Fractional bandwidth %	11.1	11.26

Chapter V

Metamaterial transmission line with negative magnetic coupling

In this chapter a metamaterial transmission line with negative magnetic coupling is presented. First, the theoretical analysis of the metamaterial transmission line using negative magnetic coupling is shown. Then, the design of metamaterial transmission line (MTM) using planar technology is offered. A spiral inductor and interdigital capacitor are used as basic elements to realize the MTM transmission line. A detailed design procedure, operation regions, and equivalent circuit of the spiral inductor and interdigital capacitor are explained. Finally, the simulated and measured transmission and reflection parameters of the MTM transmission line are presented.

5.1 Metamaterial with negative magnetic coupling

In [4] a MTM unit-cell based on serial capacitors connected to magnetically negative-coupled inductors is proposed. A unit-cell is a basic building block of the structure that can be used to reproduce the entire structure. A metamaterial is a periodic structure composed of many unit-cells, ideally of an infinite number of cells. A metamaterial must satisfy the homogeneity condition; this condition states that the physical length of the unit-cell must be smaller than a quarter of the wavelength associate to the frequency applied to the material. In other words, the phase variation of a wave on the edges of the unit-cell must be smaller than 90° ($|\Delta\phi| < \pi/2$). A metamaterial is called a perfectly homogeneous material if $|\Delta\phi| << \pi/2$. Figure 5.1 shows a periodic

structure composed of unit-cells. *M* represents the mutual inductance between the adjacent inductors, “a” stands for the unit-cell length.

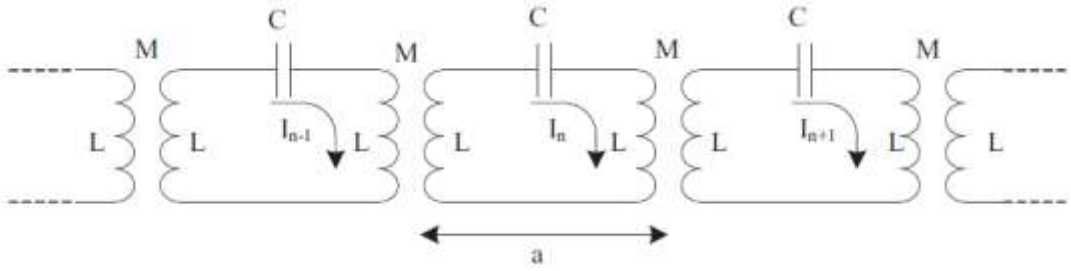

Figure 5.1. One-dimension network magnetically coupled [35].

The unit-cell can begin and end with many different points as long as the structure composed of these cells remains being periodic. Figure 5.2 shows two possible unit-cells of the periodic structure shown in Figure 5.1

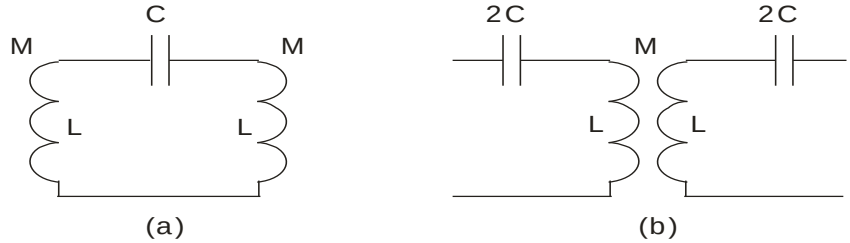

Figure 5.2. Two different unit-cells for the periodic structure.

The structure was mathematically proven to be metamaterial; the dispersion relation is associated to equation (5.1a), and equation (5.1b) is associated to the product of phase and group velocity.

$$\omega^2(k) = \frac{1}{2C(L + M\cos(ka))} \tag{5.1a}$$

$$v_g v_p \cong \frac{Ma^2}{4(L+M)^2 C} \tag{5.1b}$$

where *k* is the wave vector, *C* is the capacitor value, *L* is the inductor value, *M* is the mutual inductance value, and *a* is the-unit cell length.

M can be positive or negative. Based on the dispersion relation equation the change of sign for *M* implies that the wave goes from forward to backward. From the product of phase and group velocity, if *M* is positive the velocities are parallel, if *M* is negative the velocities are anti-parallel. The dispersion relations for *M* positive and negative are shown in Figure 5.3. It can be seen that the dispersion relation is reversed with the change of sign of *M*, but the frequency range does not change.

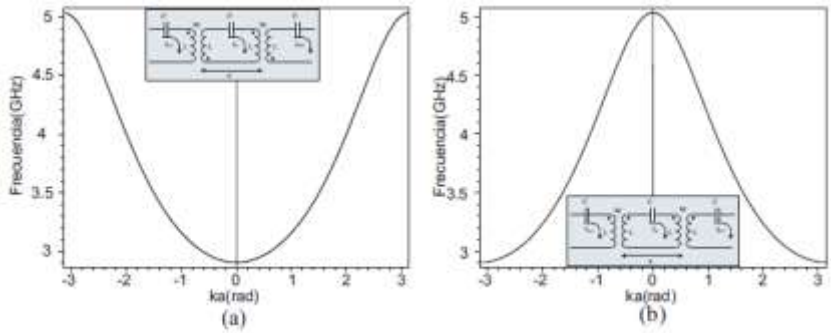

Figure 5.3. Dispersion relation for the 1D system with *C* = 0.1 pF, *L* = 10 nH and (a) *M* = 5 nH and (b) *M* = -5 nH [35].

It is concluded that when *M* is positive the structure is right-handed, and when *M* is negative the structure is left-handed. This structure is theoretically proposed. A practical implementation of this structure in microstrip technology is taken into account. A spiral inductor and interdigital capacitor are used as basic elements to realize the MTM transmission line. A detailed design procedure, operation regions, and equivalent circuit of the spiral inductor and interdigital capacitor are explained in the next sections. Figure 5.2(b) is the schematic of the unit-cell which is used for the design and fabrication.

5.2 Design of the spiral inductor

The inductance value for the spiral inductor made with microstrip lines depends on its physical dimensions. There are several equations for calculating the inductance value based on the physical dimensions. Even

though these equations have good accuracy, the actual impedance of the spiral inductor not only has an inductance value but also contains resistance and parasitic capacitance values. A related simple equation is presented in [36], this equation is

$$L = 8.5n^{5/3}\sqrt{A} \qquad (5.2)$$

where *A* is the area that is occupied by the inductor in cm^2, *n* is the number of turns, and *L* is given in nH.

A schematic of the spiral inductor is shown in Figure 5.4.

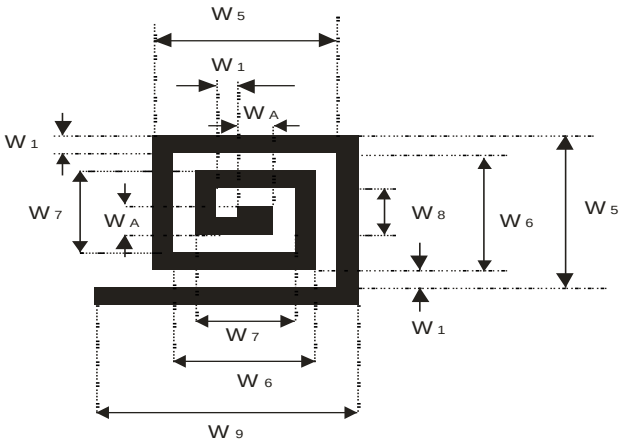

Figure 5.4. Schematic of the spiral inductor.

Simulations were performed to optimize the dimensions of the spiral inductor using a full wave simulator [29]. The dimensions of the spiral inductor are: W_1= 0.3mm, W_5= 2.6 mm, W_6= 2 mm, W_7= 1.4 mm, W_8= 0.8 mm, W_9= 3.7 mm, W_A= 0.5 mm. The theoretical and simulated values of the spiral inductor inductance are 10.003 nH and 10.2 nH respectively.

A spiral inductor has 3 operational regions,

region I is the useful band, for this region there is a small effect of parasitic capacitance, the inductance effect is dominant, the inductance value is almost constant and the structure can be used as an inductor. The

spiral inductor is fabricated using microstrip lines; there is an associated capacitance between these lines and the ground plane resulting on a parasitic capacitance for the spiral inductor.

region II there is a transition for this region, the self-resonance of the inductor is present as a consequence of the electric and magnetic energies being identical. When this occurs, the value of the inductance drops to zero and the structure can no longer be used as an inductor.

region III the reactance value goes from positive to negative because the capacitive effect becomes dominant, the magnetic energy is surpassed by the electric energy, and as a consequence no magnetic energy can be transmitted to nearby components.

The inductor area, number of turns and metal traces width are the key parameters for increasing the self-resonant frequency, as they decrease the self-resonant frequency increases. Figure 5.5(a) presents the three regions of the spiral inductor. The spiral inductor can be modeled as shown in Figure 5.5(b), where R_S is the resistance of the metal traces and C_p is the parasitic capacitance.

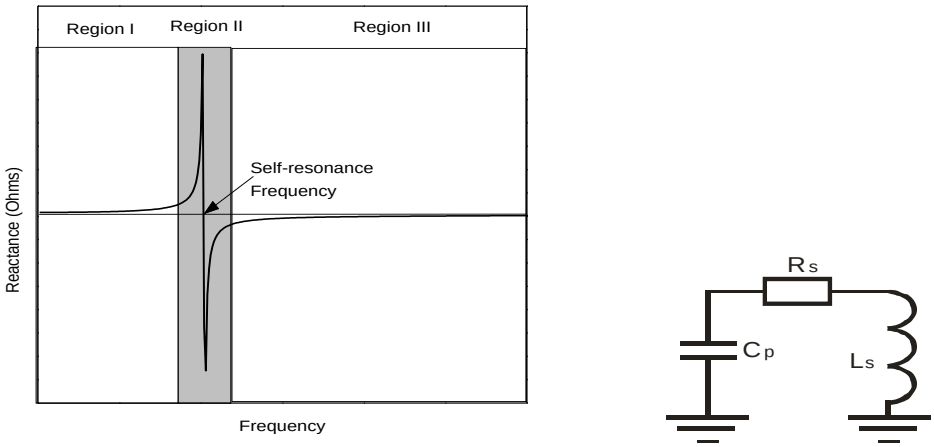

(a) (b)

Figure 5.5. (a) Regions of the spiral inductor and (b) equivalent circuit of spiral inductor.

The values for R_S and C_p were obtained with the procedure presented in [37]. The substrate used for designing the spiral inductors is Rogers Duroid 6010 (dielectric constant (ε_r) = 10.8, dielectric loss tangent (δ) = 0.001 and substrate thickness (h) = 0.65 mm).

The series resistance of a spiral inductor can be obtained from the Y-parameters with

$$R_S = \mathrm{Re}\left(\frac{1}{-Y_{12}}\right) \tag{5.3}$$

The shunt capacitance between the metal lines of the spiral inductor and the ground plane is represented by C_p. The conventional parallel plate calculations of capacitance value are only valid for metal lines that are wider than the dielectric thickness. Y-parameters can be used to predict the shunt capacitances with the following equations

$$C_{p1} = \frac{\mathrm{Im}(Y_{11} + Y_{12})}{2\pi f} \tag{5.4a}$$

$$C_{p2} = \frac{\mathrm{Im}(Y_{22} + Y_{21})}{2\pi f} \tag{5.4b}$$

where f is the frequency, C_{p1} and C_{p2} are the parasitic capacitances at the input and output respectively. These parasitic capacitances are approximately half the total parasitic value Cp.

5.3 Interdigital capacitor

The interdigital capacitor is a coplanar capacitor; it takes its name from its shape. The interdigital capacitor is suitable for applications where low values of capacitance are required (less than 1 pF). The calculation of its associated

capacitance requires numerical methods; this capacitor has a lower sensitivity to the substrate thickness than a conventional parallel plate capacitor. Figure 5.6 shows the field distribution for the interdigital capacitor.

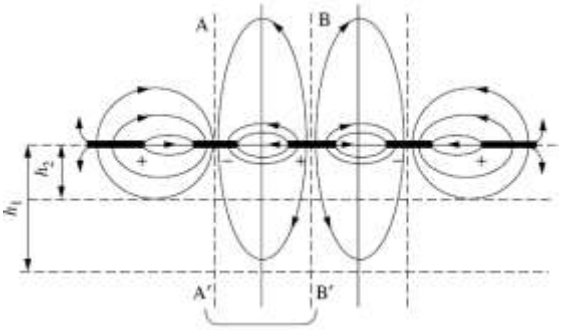

Figure 5.6. Schematic field distribution of interdigital capacitors [38].

To calculate the dimensions of the interdigital capacitor (C_2 = 1.5 pF), we use the following equations [39]

$$C_2 = \frac{\varepsilon_r + 1}{W} l((N-3)A1 + A2) \text{ pf/in} \quad (5.5a)$$

$$A_1 = \left[0.3349057 - 0.15287116\left(\frac{t}{x}\right) \right]^2 \text{ pf/in} \quad (5.5b)$$

$$A_2 = \left[0.50133101 - 0.22820444\left(\frac{t}{x}\right) \right]^2 \text{ pf/in} \quad (5.5c)$$

where t is the metal thickness, x is the line width, N is the number of fingers, l is the finger length, W is the total capacitor width, and ε_r is the effective permittivity.

The layout of the interdigital capacitor is shown in Figure 5.7(a). The dimensions of the interdigital capacitor are given as: x = 0.3 mm, l = 3.8 mm, W = 5.7 mm, t = 15 μm, N = 10, and ε_r = 10.8. The main electromagnetic field of the interdigital capacitor is the one on the plane (C_2), but there are parasitic effects. An equivalent circuit for the interdigital capacitor is depicted in Figure

5.7(b). C_1 represents the shunt capacitance associate to the microstrip lines and R_{s1} represents the serial resistance of the lines, due to the metal resistivity.

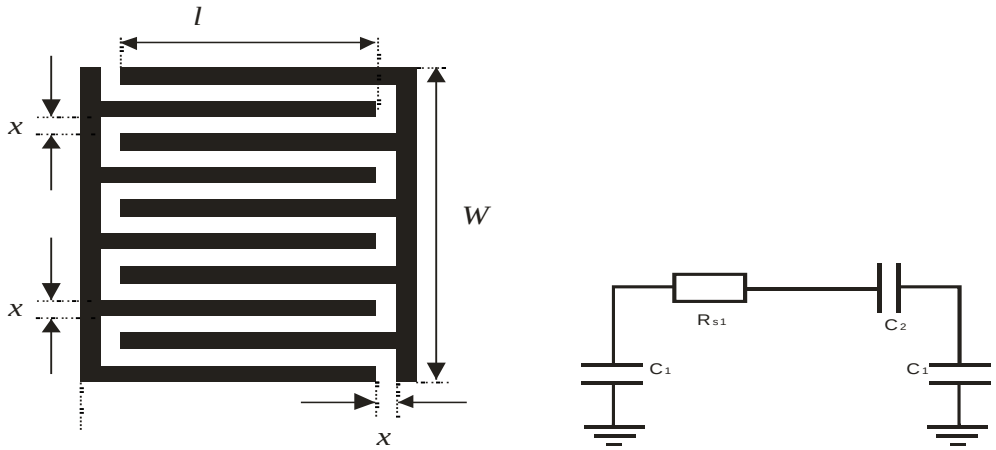

(a) (b)

Figure 5.7. (a) Layout and (b) equivalent circuit of interdigital capacitor.

5.4 Negative magnetic coupling in Spiral Inductors

The spiral inductor as mentioned before has a self-resonance, when this structure is close enough to another structure, the electromagnetic interaction between them is noticeable. The interaction causes that the resonance peaks of the structures change their respective values, the interaction is known as coupling coefficient *´k´*. Using two identical value inductors we seek negative magnetic coupling, coupling between lines depends on the line proximity, the coupling can be positive or negative, Figure 5.8 presents both cases, “A” and “B” represents the inductors. When both inductors are wired in the same direction a positive mutual inductance is obtained; whereas, a negative mutual inductance is achieved whit opposite wiring direction.

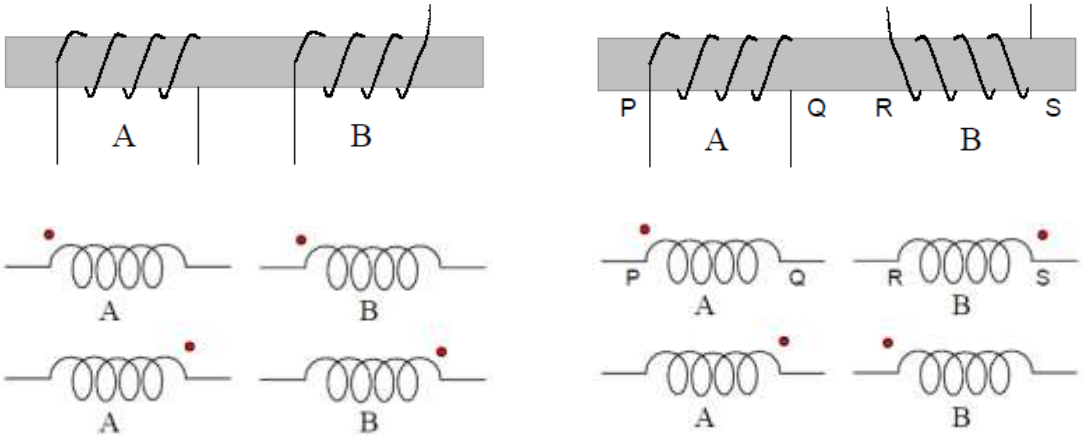

(a) (b)

Figure 5.8. (a) Positive coupling and (b) negative coupling.

The coupling coefficient between the two resonators *k* is found using

$$k = \pm \frac{f_2^2 - f_1^2}{f_2^2 + f_1^2} \tag{5.6}$$

where f_2 denotes the higher frequency peak value and f_1 the lower frequency peak value [33].

Mutual inductance and magnetic coupling are related by

$$M = k\sqrt{L_1 L_2} = kL \tag{5.7}$$

where L_1 and L_2 are the values for inductor 1 and 2, and as the values are identical, they both are denoted by *L*.

Using equation (5.6), with a separation between spiral inductors of 0.2 mm, the magnetic coupling value is *k* = -0.1258. If the value of the inductors is 10.2 nH, then using equation (5.7) the mutual inductance value is *M* = -1.28 nH. Figure 5.9 shows the circuit layout of the magnetic-coupled spiral inductors.

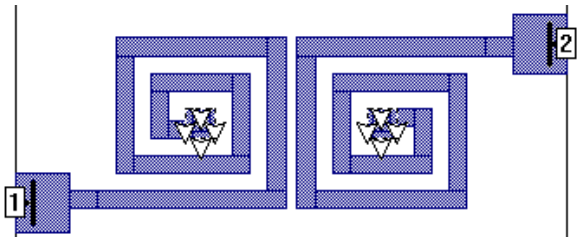

Figure 5.9. Layout of spiral inductors with magnetic coupling.

The *S*-parameter magnitudes for the circuit presented in Figure 5.2(b) are identical if *M* is positive or if *M* is negative, as a matter of fact, S_{11} parameters do not change if just *M* changes sign. S_{21} parameters magnitudes are equal but the phases are different. We use the notation + to indicate that *M* is positive and – for *M* negative. The *S*-parameters for positive and negative magnetic coupling, are related as

$$|S_{11+}|(dB) = |S_{11-}|(dB) \tag{5.8a}$$

$$|S_{21+}|(dB) = |S_{21-}|(dB) \tag{5.8b}$$

$$S_{11+}(\phi) = S_{11-}(\phi) \tag{5.8c}$$

$$S_{21+}(\phi) \neq S_{21-}(\phi) \tag{5.8d}$$

$$S_{21+}(\phi) = S_{21-}(\phi - \pi) \tag{5.8e}$$

$$\mathrm{Re}(S_{21+}) = -\mathrm{Re}(S_{21-}) \tag{5.8f}$$

$$\mathrm{Im}(S_{21+}) = -\mathrm{Im}(S_{21-}) \tag{5.8g}$$

In order to validate the above equations, simulations were performed using the proposed structure shown in Figure 5.2(b), the values are: C = 0.1 pF, L = 10 nH, and M = ± 5 nH. Simulated reflection and transmission coefficient responses of the proposed structure are depicted in Figures 5.10, 5.11, and 5.12.

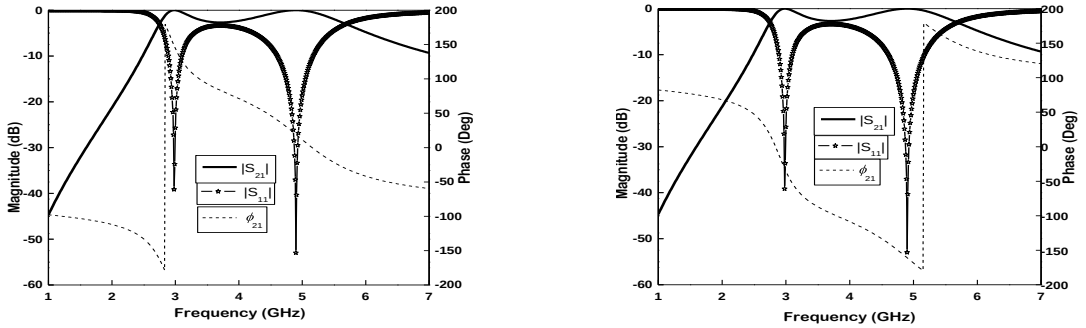

(a) (b)

Figure 5.10. Magnitude and phase of the transmission and magnitude of the reflection when *M* is (a) negative and (b) positive.

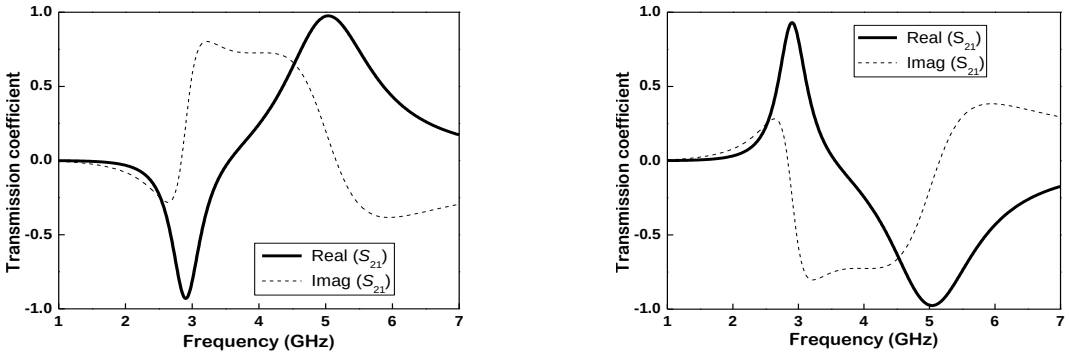

(a) (b)

Figure 5.11. Real and imaginary parts of the transmission when *M* is (a) negative and (b) positive.

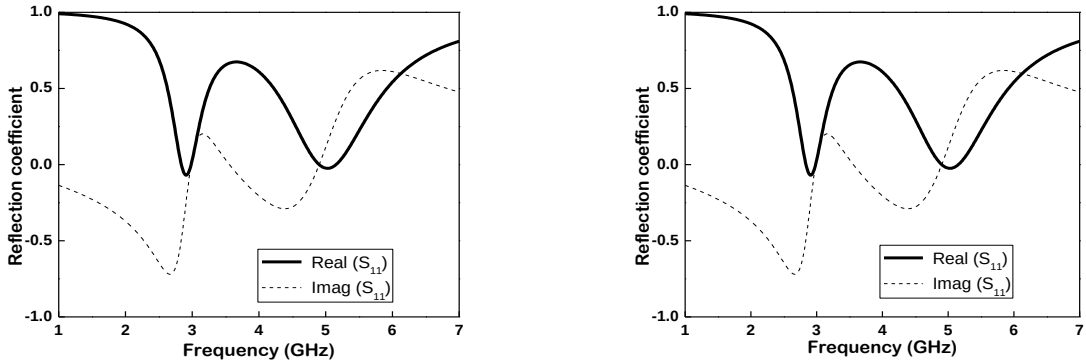

(a) (b)

Figure 5.12. Real and imaginary parts of the reflection when *M* is (a) negative (b) positive.

5.5 Metamaterial Transmission Line using Negative magnetic coupling and Effective Parameter Extraction

In [40] there is a forward wave transmission for the axial line distribution, and there is a backward wave transmission for a planar line distribution, i.e. there is a phase delay for the rings which are axially distributed, and a phase advance for rings with planar distribution. To verify if the proposed structure has metamaterial behavior, the effective parameters are taken into account. The extraction procedure is used to provide effective permittivity and effective permeability values of a given structure. There are several methods for the extraction, the most popular approach is the extraction from the reflection and transmission characteristics. The effective permittivity (ε_{eff}), effective permeability (μ_{eff}), and propagation constant for the MTM TL unit-cell, were extracted from the simulated *S*-parameters using the procedure described in [41]. The simulated structure is shown in Figure 5.13.

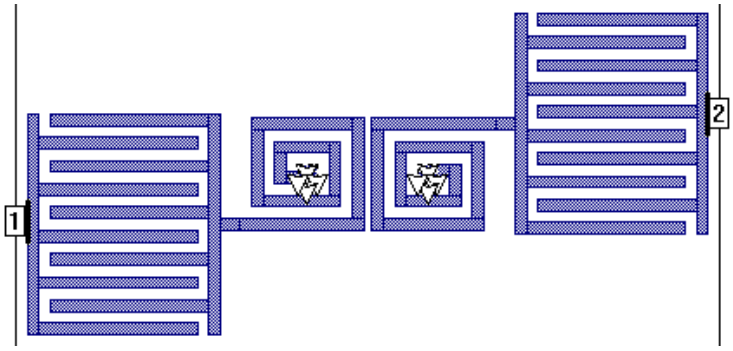

Figure 5.13. Simulated structure for parameter extraction.

The procedure used for extracting the effective parameters is as follows: The *S*-parameters are related with the transmission and reflection coefficients by

$$S_{11} = \frac{\Gamma(1-T^2)}{1-\Gamma^2 T^2} \tag{5.9a}$$

$$S_{21} = \frac{T(1-T^2)}{1-\Gamma^2 T^2} \tag{5.9b}$$

where the normalized-to-Z_0 transmission and reflection coefficients

$$\Gamma = \frac{(Z_{sn}-1)}{(Z_{sn}+1)} \tag{5.10a}$$

$$T = e^{-\gamma d} \tag{5.10b}$$

where *d* is the total length of the unit-cell along the propagation direction, γ is the propagation constant of the unit-cell, and Z_{sn} is the normalized characteristic impedance. γ and Z_{sn} are related to ε^* and μ^* (the complex conjugates of ε and μ) by

$$\gamma = \gamma_0 \sqrt{\varepsilon^* \mu^*} \tag{5.11a}$$

$$Z_{sn} = \sqrt{\frac{\mu^*}{\varepsilon^*}} \tag{5.11b}$$

where $\gamma_0 = (j2\pi/\lambda_0)$ is the propagation constant of free space, λ_0 is the wavelength for free space. From equations (5.9a) and (5.9b), Γ and *T* are represented in terms of the *S*-parameters as

$$\Gamma = K \pm \sqrt{K^2 - 1} \tag{5.12}$$

where

$$K = \frac{S_{11}^2 - S_{21}^2 + 1}{2S_{11}} \tag{5.13a}$$

$$T = \left(\frac{S_{11} + S_{21} - \Gamma}{1-(S_{11}+S_{21})\Gamma} \right) \tag{5.13b}$$

The ambiguity of sign for equation (5.12) is solved taking into consideration the restriction $|\Gamma|<1$. The complex propagation constant is extracted from (5.10b), and it is

$$\gamma = \frac{\ln(1/T)}{d} \tag{5.14}$$

From equations (5.10a) and (5.11b), the following equation is obtained

$$\sqrt{\frac{\mu^*}{\varepsilon^*}} = \left(\frac{1+\Gamma}{1-\Gamma}\right) \tag{5.15}$$

And from equations (5.11a) and (5.15)

$$\varepsilon^* = \frac{\gamma}{\gamma_0}\left(\frac{1-\Gamma}{1+\Gamma}\right) \tag{5.16a}$$

$$\mu^* = \frac{\gamma}{\gamma_0}\left(\frac{1+\Gamma}{1-\Gamma}\right) \tag{5.16b}$$

The parameter *T* in equation (5.14) is a complex number, as a consequence γ may have multiple values. If *T* is defined as

$$T = |T|e^{j\phi} \tag{5.17}$$

then, *γ* is given by

$$\gamma = \frac{\ln(1/T)}{d} + j\frac{2\pi n - \phi}{d} \tag{5.18}$$

where $n = 0, \pm1, \pm2, \ldots$

The dispersion relation from the *S*-parameters can be obtained by

$$\beta p = \cos^{-1}\left(\frac{1 - S_{11}S_{22} + S_{12}S_{21}}{2S_{21}}\right) \tag{5.19}$$

The MTM TL unit-cell shown in Figure 5.13 was simulated using the full-wave EM simulator [29]. The substrate used has a dielectric constant (ε_r) value of 10.8 and thickness of 0.635 mm. The previously mentioned extraction procedure is applied to the simulated structure. The extracted effective permittivity values (ε_{eff}), the effective permeability values (μ_{eff}), the propagation constant and the refraction index values for the MTM TL unit-cell are shown in Figure 5.14 (a), 5.14 (b), 5.15 (a) and 5.15 (b) respectively. As can be seen from Figure 5.14, there is a frequency region when the real effective permittivity values and the real effective permeability values are both negative, and this region is called a double negative (DNG) region. The theory discussed earlier in Chapter 2 establishes that for a DNG region the refraction index is negative. Then, it has been proven that the unit-cell is a metamaterial structure.

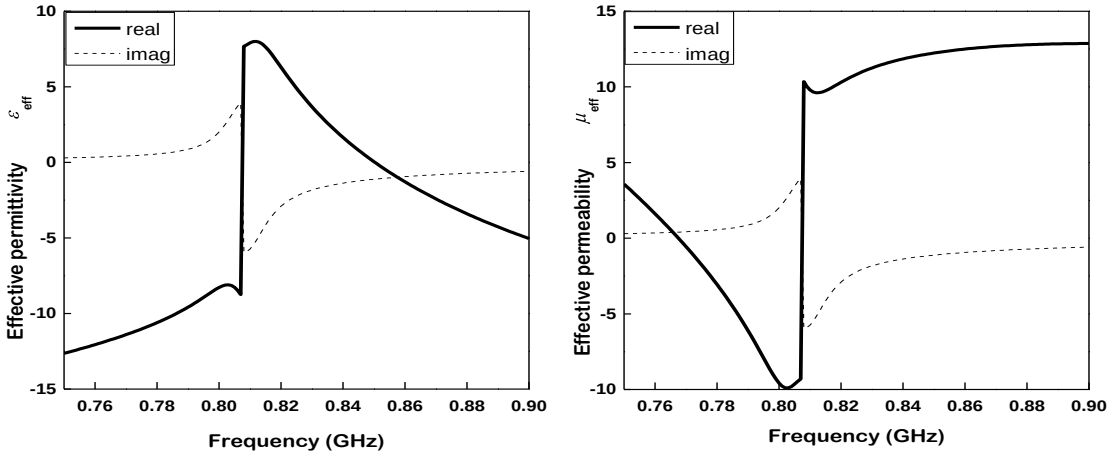

(a) (b)

Figure 5.14. Extracted values of the unit-cell (a) effective permittivity and (b) effective permeability.

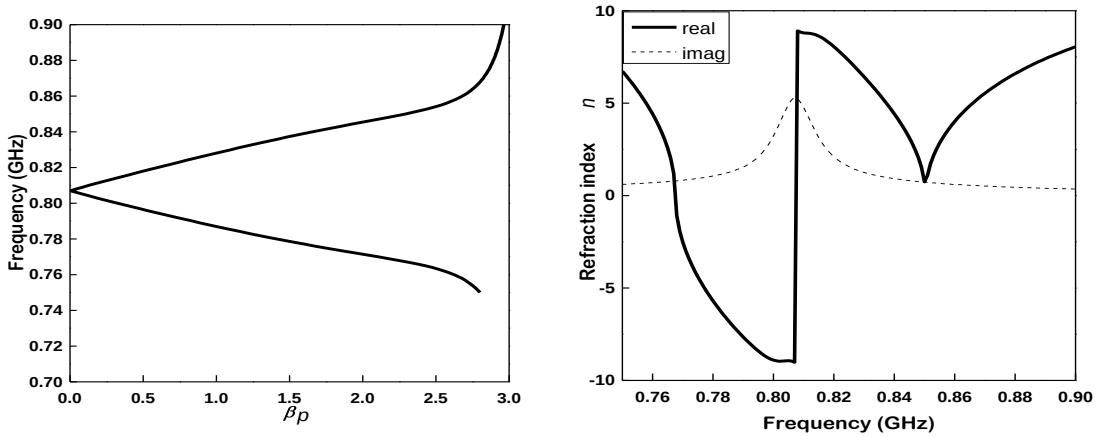

(a) (b)

Figure 5.15. (a) Extracted dispersion diagram of the unit-cell. (b) Refraction index for the unit-cell.

5.6 Results and Discussion

To validate the proposed structure, it was simulated in SONNET [29] and fabricated using a serigraphy process. Figure 5.16 presents the photograph of the fabricated circuit. The chosen substrate is Rogers Duriod-6010 with dielectric constant ε_r = 10.8, dielectric loss tangent δ = 0.001, and substrate thickness h = 0.635 mm. For the requirement of 50 Ω impedance, the width of the strip is 0.6 mm. The total dimensions of the unit-cell without connectors and feed lines are: 17.6 x 8.3 mm^2. The dimensions of the feed lines are: line width 0.6 mm and line length 4.0 mm. Measurements are performed using the Agilent PNA series microwave vector network analyzer (E8361A). Simulated and measured S_{21} frequency responses for the MTM unit-cell are presented in Figure 5.17(a). Simulated and measured insertion losses at the central frequency are 2.5 dB and 5 dB respectively. Measured and simulated S_{11} frequency responses for the MTM unit-cell are shown on Figure 5.17(b). The reflection losses for the central frequencies are: 17 dB for simulated (0.81 GHz), and 22 dB for measured (0.84 GHz). The extracted effective

permittivity and effective permeability from the measured and simulated S-parameters of the proposed unit-cell are shown in Figure 5.18(a) and Fig. 5.18(b) respectively. The discrepancy between simulated and measured values is due to the material tolerances and fabrication errors. The simulated and measured phase constants of the MTM TL are obtained from the corresponding *S*-parameters and are shown in Figure 5.19. From Figure 5.19, it is clear that there is a phase advance for the simulated unit-cell until 807 MHz, and a phase advance for the measured unit-cell until 776 MHz.

Figure 5.16. Photograph of the fabricated unit-cell.

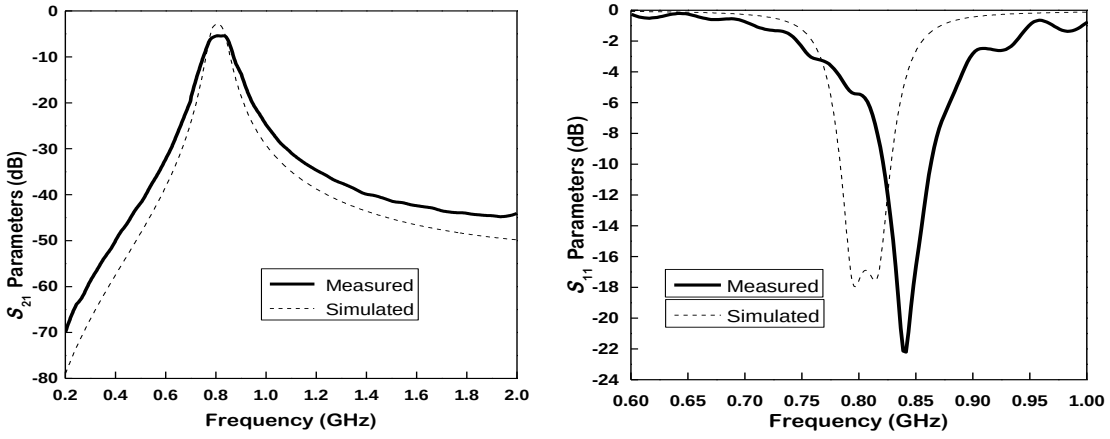

(a) (b)

Figure 5.17. Measured and simulated *S*-parameters in dB (a) S_{21} and (b) S_{11}.

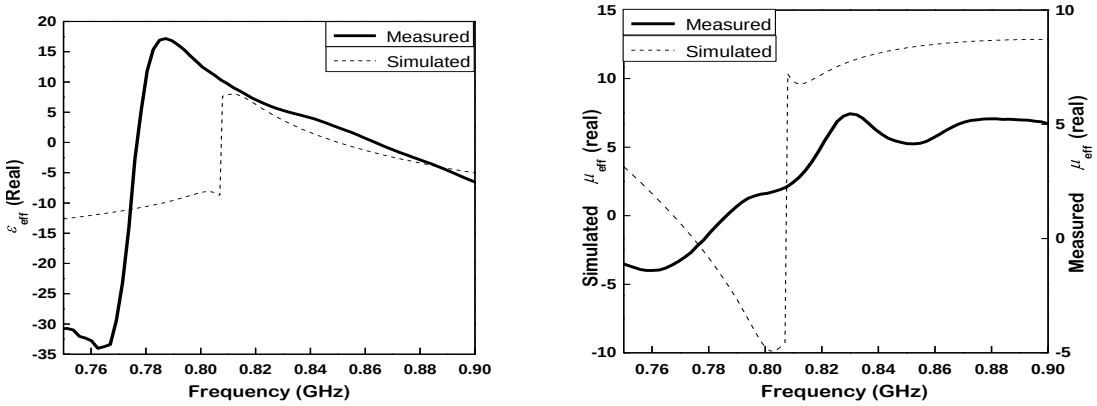

(a) (b)

Figure 5.18. Effective measured and simulated parameters (a) real part of ε_{eff} and (b) real part of μ_{eff}.

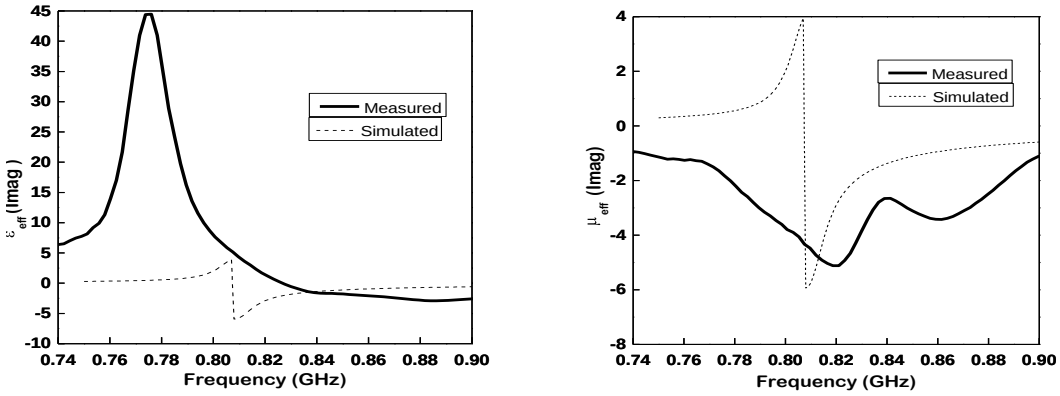

(a) (b)

Figure 5.19. Effective measured and simulated parameters (a) imaginary part of ε_{eff} and (b) imaginary part of μ_{eff}.

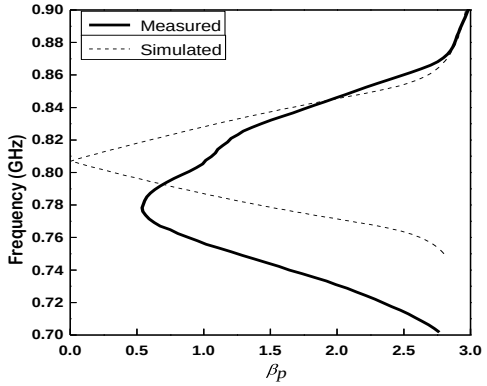

Figure 5.20. Extracted phase constant from measured and simulated results.

Chapter VI

Conclusions

In this thesis novel resonators based on via-to-ground and interdigital capacitors have been introduced. The use of via-to-ground and interdigital capacitors provides both size reduction and low sensitivity to substrate thickness. EM simulations were performed to derive the number of interdigital-capacitor fingers for which the close and open ring would have the lowest sensitivity to substrate thickness. The lowest SSTs are: 0.46%/mm for the close ring (with an eleven-finger interdigital capacitor) and 0.23%/mm for the open ring (with a fifteen-finger interdigital capacitor). A size reduction of 73% is obtained for the close ring, whereas in the case of the open ring it is 82%.

Two-pole Butterworth and Chebyshev filters were designed using the miniaturized novel ring resonator. Coupled lines and tapped lines were utilized to provide the external coupling. It is found that for the Butterworth filter a high rejection to stop band, with reflection losses below 18 dB at the central bandpass is observed. In the case of the Chebyshev filter, there was a high selectivity for the upper stopband but the insertion band turned out to be asymmetrical.

A four-pole Quasi-elliptic filter was designed and fabricated using the novel resonator. The proposed filter has high selectivity and proved to have good rejection to the stopband. Simulated and measured scattering parameters are in good agreement.

Table 6.1 presents the simulated and measured reflection coefficient, transmission coefficient, central frequency and the fractional bandwidth values of the Butterworth, Chebyshev and Quasi elliptic filters along with the

frequency shift among measured and simulated structures. Measured and simulated values are scarcely different. The differences between simulated and measured values for the main filter characteristics are attributed to the fabrication process. As can be appreciated on the photographs of the fabricated structures line widths and separation among lines are not equal at all points. Better results can be obtained with a more accurate fabrication process even when the results are in good agreement. For the Chebyshev and Quasi-elliptic filter the respective simulated and measured fractional bandwidths are very similar. The different bandwidths would scarcely affect the results due to the differences are 1.3 and 0.89% respectively. For the Butterworth filter the bandwidth difference is 18% which would greatly affect the results. The central frequency for the Butterworth and Quasi-elliptic filter are almost the same and as a consequence their respective frequency shifts are almost equal, this implies that a frequency shift percent factor can be obtained to optimized future structures.

Table 6.1. Comparison between simulated and measured values of the three filters.

	Butterworth		**Chebyshev**		**Quasi-elliptic**	
	Simulated	Measured	Simulated	Measured	Simulated	Measured
Central frequency (GHz)	0.531	0.489	0.38	0.354	0.546	0.506
Insertion loss (dB)	2.23	2.3	1.51	2.2	1.77	1.88
Reflection loss (dB)	18	25	15.05	12.64	21.35	13.81
Fractional bandwidth (%)	6.1	5	14.6	14.4	11.1	11.2
Frequency shift (GHz)	0.042		0.026		0.04	

The filters are based on resonators which are highly miniaturized, inexpensive, easily fabricated, of low sensibility to differences in the

substrate's thickness, and independent of the excitation orientation fulfilling the first objective of this thesis.

A metamaterial transmission line based on the negative magnetic coupling was fabricated using planar technology accomplishing the second objective of this thesis. Spiral Inductors and interdigital capacitors were used as the building blocks of the transmission line. Negative magnetic coupling was achieved by using the mutual coupling between the spiral inductors. The designed structure was optimized using a full-wave simulator (SONNET). Effective parameter extraction was performed to provide effective permittivity and effective permeability values of the simulated structure to verify metamaterial behavior. Simulated and measured insertion losses at the central frequency were 2.5 and 5 dB respectively. For the reflection losses the simulated value was 17 dB and the measured value was 25 dB. The discrepancy between simulated and measured values is attributed to the fabrication process material tolerances. The effective permittivity and permeability have negative values in the frequency range from 770 to 807 MHz for the simulated structure whereas for the fabricated structure it was 740 to 776 MHz. The simulated and fabricated structure showed similar behavior, but the losses of the fabricated structure were relatively high. The high losses would do impractical to place more than 2 unit-cells, in addition the phase constant do not reach the value zero delimiting the possible phase advance values that the structure can provide. One advantage of metamaterial structures is the size reduction. It is noticed that a high magnetic coupling coefficient is a key factor to obtain transmission lines with high bandwidth.

Figure index

Table index

References

[1] L. Liu, C. Caloz, and T. Itoh, “Dominant mode leaky wave antenna with ba ck-to-endfire scanning capability,” *Electronic letters*, vol. 38, pp. 1414-1416, November 2002.

[2] F. Falcone, F. Martín, J. Bonache, R. Marqués, T. Lopetegi, and M. Sorolla, “Left handed coplanar waveguide band pass filters based on bi-layer split ring resonators,” *IEEE microwave and wireless components letters*, vol. 14, no. 1, pp. 10-12, January 2004.

[3] J. Bonache, I. Gil, J. Garcia-Garcia, and F. Martin, “Novel microstrip band pass filters based on complementary split ring resonators,” *IEEE Trans. on microwave theory and techniques*, vol. 54, no. 1, pp. 265–271, January 2006.

[4] U. Algredo-Badillo and P. Halevi, “Negative refraction and focusing in magnetically coupled L-C loaded transmission lines,” *Journal of Applied Physics,* vol. 102, no. 8, pp. 086104.1-086104.3, 16 Oct 2007.

[5] I. Wolff, and N. Knoppik, “Microstrip ring resonator and dispersion measurement on microstrip lines,” *Electronics Letters.,* vol. 7, no. 26, pp. 779-781, December 1971.

[6] K. Chang, and L. H. Hsieh, “Microwave ring circuit and related structures,” *second edition, Wiley*, New Jersey, 2004.

[7] I. Wolff, “Microstrip bandpass filter using degenerate modes of a microstrip ring resonator,” *Electronics Letters,* vol. 8, no. 12, pp. 302-303, June 1972.

[8] L. H. Hsieh, and K. Chang, “Compact dual-mode elliptic-function bandpass filter using a single ring resonator with one coupling gap,” *Electronic letters*, vol. 36, no. 19, pp. 1626-1627, September 2000.

[9] A. Gorur, “A novel dual-mode bandpass filter with wide stopband using the properties of microstrip open-loop resonator,” *Microwave and wireless components lett*ers, vol. 12, no. 10, pp. 386-388, October 2002.

[10] L. H. Hsieh, and K. Chang, “Dual-mode quasi-elliptic-function bandpass filter using ring resonators with enhanced-coupling tuning stubs,” *Transactions on microwave theory and techniques*., vol. 50, no. 5, pp. 1340-134, May 2002.

[11] V. Veselago, “The electrodynamics of substances with simultaneously negative values of ε and μ,” *Soviet Physics Uspekhi*, vol. 10, no. 4, pp. 509-514, Jan., February 1968.

[12] Christophe Caloz, and Tatsuo Itoh, “Metamaterials: Transmission line theory and microwave applications,” *Wiley*, New Jersey, 2006.

[13] W. J. Padilla, D. N. Basov, D. R. Smith, “Negative refractive index metamaterials,” *materials today*, vol. 9, no. 7-8, pp. 28–35, July-August 2006.

[14] R. A. Shelby, D. R. Smith, and S. Schultz, “Experimental verification of a negative index of refraction,” *Science*, vol. 292, pp. 77-79, April 2001.

[15] G. V. Eleftheriades, A. K. Iyer, P. C. Kremer, “Planar negative refractive index media using periodically *L-C* loaded transmission lines,” *IEEE Trans. on microwave theory and techniques*, vol. 50, no. 12, pp. 2702-2712, December 2002.

[16] A. Grbic, G. V. Eleftheriades, “Negative refraction, growing evanescent waves, and sub-diffraction imaging in loaded transmission-line metamaterials,” *IEEE Trans. on microwave theory and techniques*, vol. 51, no. 12, pp. 2297-2305, December 2003.

[17] A. Grbic, G. V. Eleftheriades, “Experimental verification of backward-wave radiation from a negative refractive index metamaterial,” *Journal of applied physics*, vol. 92, no. 10, pp. 5930-5935, November 2002.

[18] C. Caloz, T. Itoh, “Novel microwave devices and structures based on the transmission-line approach of meta-materials,” *in Microwave symposium digest, IEEE MTT-S International microwave symposium*, vol. 1, pp. 195-198, June 2003.

[19] M. Antoniades, G. V. Eleftheriades, “Compact, linear, lead/lag metamaterial phase shifters for broadband applications,” *IEEE Antennas wireless propagation letters*, vol. 2, pp. 103-106, 2003.

[20] J. Perruisseau-Carrier, A. K. Skrivervik, “Composite right/left-handed transmission line metamaterial phase shifters (MPS) in MMIC technology,” *IEEE Trans. on microwave theory and techniques*, vol. 54, no. 4, pp. 2297-2305, April 2006.

[21] S. Abielmona, S. Gupta, C. Caloz, “Experimental demonstration and characterization of tunable CRLH delay line system for impulse/continuous wave,” *IEEE microwave and wireless components lett.*, vol. 17, no. 12, pp. 864-866, December 2007.

[22] F. Martín, J. Bonache, F. Falcone, M. Sorolla, R. Marqués, “Split ring resonator-based left-handed coplanar waveguide,” *Applied physics lett.*, vol. 83, no. 22, pp. 4652-4654, December 2003.

[23] I. Arnedo, J. Illescas, M. Flores, T. Lopetegi, M.A.G. Laso, F. Falcone, J. Bonache, J. Gracia-García, F. Martín, J.A. Marcotegui, R. Marqués, M. Sorolla, “Forward and backward leaky wave radiation in split-ring-resonator-based metamaterials,” *IET Microwave antennas propag.*, vol. 1, no. 1, pp. 65-68, February 2007.

[24] Z. Xu, W. Lin, L. Kong, “Controllable metamaterial electromagnetic structure research on applying to stealth technology,” *Microwave and optical technology letters*, vol. 49, no. 7, pp. 1616-1619, July 2007.

[25] M. Antoniades, G. V. Eleftheriades, “A broadband series power divider using zero-degree metamaterial phase-shifting lines,” *IEEE Microwave guided wave lett*., vol. 15, no. 11, pp. 808–810, 2005.

[26] M. Gil, J. Bonache, J. Garcia-Garcia, J. Martel, F. Martin, “Composite right/left-handed metamaterial transmission lines based on complementary split-rings resonators and their applications to very wideband and compact filter design,” *IEEE Trans. on microwave theory and techniques*, vol. 55, no. 6, pp. 1296–1304, June 2007.

[27] M. Gil, J. Bonache, F. Martin, “Metamaterial filters with attenuation poles in the pass band for ultra wide band applications,” *Microwave and optical technology letters*, vol. 49, no. 12, pp. 2909–2913, December 2007.

[28] C. Caloz, A. Sanada, T. Itoh, “A novel composite right-/left-handed coupled-line directional coupler with arbitrary coupling level and broad bandwidth,” *IEEE Trans. on microwave theory and techniques*, vol. 52, no. 3, pp. 980–992, March 2004.

[29] Sonnet 12, *Sonnet Software Inc*.

[30] A. Corona-Chávez, C. Gutiérrez-Martínez, M.J. Lancaster, and A. Torres-Fortiz, “Novel dual-mode ring resonators with very low sensitivity to substrate thickness,” *Microwave and optical technology letters* vol. 47, pp. 381-384, 2005

[31] J. Zhou, and M. J. Lancaster, “Superconducting microstrip filters using compact resonators with double-spiral inductor and interdigital capacitors,” *IEEE MTT-S Dig* (2003), 1889-1892.

[32] J. S. Hong, and M. J. Lancaster, “Microstrip filters for RF/microwave applications,” *Wiley*, NJ, 2001.

[33] J. S. Hong, and M. J. Lancaster, “Design of highly selective microstrip bandpass filters with a single pair of attenuation poles at finite frequencies,” *Transactions on microwave theory and techniques,* vol. 48, no. 7, pp. 1098-1107, July 2000.

[34] R. Levy, “Filters with single transmission zeros at real or imaginary frequencies,” *Transactions on microwave theory and techniques,* vol. MTT-24, no. 4, pp. 172-181, April 1976.

[35] U. Algredo-Badillo “Refracción negativa y enfocamiento en líneas de transmisión L-C acopladas magnéticamente,” *Tesis de maestría*, INAOE, November 2006.

[36] S. Y. Liao , “Microwave circuit analysis and amplifier design,” *Prentice-Hall*, NJ, 1987.

[37] G.A. Lee, M. Megahed, F. De Flaviis “Design and analysis of novel compact inductors resonator filter,” *IEEE MTT Sym Dig (2002),* Seattle, Wa, pp. 1621-1624.

[38] L. F. Chen, C. K. Ong, C. P. Neo, V.V. Varadan, and V. K. Varadan, “Microwave electronics measurement and material characterization,” *Wiley*, England, 2004.

[39] B. C. Wadell, “Transmission line design handbook,” *Artech House* pp. 420-422.

[40] M. C. K. Wiltshire, E. Shamonina, I. R. Young, and L. Solymar, “Dispersion characteristics of magneto-inductive waves: comparison between theory and experiment,” *Electronics Letters.,* vol. 39, no. 2, pp. 215-217, January 2003.

[41] G. Lubkowski, R. Schuhmanm, and T. Weiland, “Extraction of effective metamaterial parameters by parameters fitting of dispersive models,”

Microwave and technology letters, vol. 49, no. 2, pp. 285-288, February 2007.